

Interface shape surrounding anisotropic particles held at the liquid-gas interface

Avital Reizman Einhorn^{1,†}, Jibu Tom Jose^{1,†}, Anna Zigelman^{1,†}, Amir Daniel Gat¹ and Omri Ram¹

¹Faculty of Mechanical Engineering, Technion – Israel Institute of Technology, Haifa 3200003, Israel **Corresponding authors:** Omri Ram, omri.ram@technion.ac.il; Amir Daniel Gat, amirgat@technion.ac.il

(Received 5 November 2024; revised 22 July 2025; accepted 15 September 2025)

Floating particles deform the liquid–gas interface, which may lead to capillary repulsion or attraction and aggregation of nearby particles (e.g. the Cheerios effect). Previous studies employed the superposition of capillary multipoles to model interfacial deformation for circular or ellipsoidal particles. However, the induced interfacial deformation depends on the shape of the particle and becomes more complex as the geometric complexity of the particle increases. This study presents a generalised solution for the liquid-gas interface near complex anisotropic particles using the domain perturbations approach. This method enables a closed-form solution for interfacial deformation near particles with an anisotropic shape, as well as the varying height of the pinned liquid-gas contact line. We verified the model via experiments performed with fixed particles held at the water level with shapes such as a circle, hexagon and square, which have either flat or sinusoidal pinned contact lines. Although in this study we concentrate on the equilibrium configuration of the liquid-gas interface in the vicinity of particles placed at fixed positions, our methodology paves the way to explore the interactions among multiple floating anisotropic particles and, thus, the role of particle geometry in self-assembly processes of floating particles.

Key words: interfacial flows (free surface), contact lines

1. Introduction

The study of floating objects has garnered attention since the middle of the 20th century due to various practical applications. These include the use of colloidal particles to

[†]These authors contributed equally to this work.

[©] The Author(s), 2025. Published by Cambridge University Press. This is an Open Access article, distributed under the terms of the Creative Commons Attribution licence (https://creativecommons.org/licenses/by/4.0/), which permits unrestricted re-use, distribution and reproduction, provided the original article is properly cited.

stabilise emulsions (Binks & Horozov 2006; Tavacoli *et al.* 2012), the ability of insects and spiders to move on water surfaces (Gao & Jiang 2004; Bush & Hu 2006) and capillary-driven self-assembly involving particles floating at a liquid–air interface (Whitesides & Boncheva 2002; Whitesides & Grzybowski 2002; Delens, Collard & Vandewalle 2023). Liquid–air interface deflections by partially wet ellipsoids are known to cause chaining (Loudet *et al.* 2005, 2006; van Nierop, Stijnman & Hilgenfeldt 2005; Lewandowski *et al.* 2008) and result in aggregates of particles with complex shapes and selectively functionalised faces, which can be used to create tuneable devices like lenses with adjustable focal lengths (Bucaro *et al.* 2009).

Self-assembly processes of objects that float on the surface of a liquid are driven by local liquid interface deformation around the objects, which depends on their shape, buoyancy and wetting properties (Kralchevsky & Nagayama 1994; Danov & Kralchevsky 2010; Gat & Gharib 2013; Poty, Lumay & Vandewalle 2014). Based on the calculations of the surface height in the neighbourhood of a single bubble at rest on a horizontal surface of a fluid, Nicolson (1949) examined the implications of the fluid–fluid interface distortions for bubble–bubble interactions in particle rafts. Chan, Henry & White (1981), Kralchevsky & Denkov (2001) and Vella & Mahadevan (2005) found that the resulting shape of the liquid surface elevation, which was previously studied by Nicolson (Nicolson 1949), causes the attraction/repulsion between bubbles.

Interaction between two floating particles occurs when the distance between them is of the order of the capillary length. For similar particles with similar capillary lengths, this means that the regions of interface deformation caused by each particle overlap, lead to mutual interaction (Loudet, Yodh & Pouligny 2006). Particles with similar wetting properties and shapes tend to attract one another and form floating aggregates (Kralchevsky & Nagayama 2000). Lucassen (1992) showed theoretically that interparticle interaction will take place as soon as the regions with deformed surfaces around two adjoining particles begin to overlap, where this interaction was calculated for particles with wetting perimeters of a sinusoidal shape. Yao et al. (2013) studied particles at interfaces with contact-line undulations having a wavelength significantly smaller than the characteristic particle size. By using theory and experiment, they showed that identical microparticles with features in phase attract each other, and microparticles with different wavelengths, under certain conditions, repel each other in the near field, leading to a measurable equilibrium separation. Equilibrium and mutual attraction or repulsion of objects supported by surface tension were also studied by Mansfield, Sepangi & Eastwood (1997). These phenomena are commonly called the Cheerios effect and were highlighted by Vella & Mahadevan (2005) as well, who discussed some examples of particles' attraction and repulsion taking into account their weight and buoyancy. Capillary interactions between particles trapped at the interface have been widely studied, both experimentally and theoretically. Botto et al. (2012) provides a comprehensive discussion of the physical mechanisms governing interface deformations around anisotropic particles and their resulting pairwise interactions. More recently, Forth et al. (2019) expanded this by highlighting how such interactions can be harnessed to design dynamic and reconfigurable assemblies at complex liquid interfaces, connecting fundamental physics to functional material architectures. These studies emphasise the central role of interface shape in determining particle interactions and configurations.

Singh & Joseph (2005) proposed a direct numerical simulation method to describe the nonlinear mechanism of capillary attraction between floating particles. Based on level sets, their numerical scheme allowed them to simulate the evolution of single spheres and disks to their equilibrium depth and the evolution to clusters of two and four spheres and two disks under capillary attraction. The interaction between adjacent

floating particles may also be explained by using an analogy between capillary and electrostatic forces. Attachment of particles is introduced by 'capillary charges' referred as poles (Kralchevsky & Nagayama 2000; Kralchevsky & Denkov 2001; Danov et al. 2005; Danoy & Kralchevsky 2010), which characterise the magnitude of the interfacial deformation and could be both positive and negative. For multipoles, the sign and magnitude of the capillary force depend on the interplay between the curvature signs of the interfacial deformations in the vicinity of the interacting particles. Capillary multipoles have been experimentally investigated by Bowden et al. (1997, 1999) and Wolfe et al. (2003), who observed that particles located along an interfacial surface meniscus with the same sign attract one another, while those along a meniscus with opposite signs repel one another. The strength and directionality of the interactions can be tailored by manipulating the heights of the faces, the pattern of the hydrophobic/hydrophilic faces and the densities of the three interacting phases. In a recent study, Eatson et al. (2024) explored the impact of particle shape on both short-range and long-range interactions by using colloidal building blocks composed of polygonal plates with uniform surface chemistry and wavy edges. Utilising minimum energy calculations alongside Monte Carlo simulations, which defined the interaction potential through multipoles, they showcased how colloidal building blocks could be customised to form diverse two-dimensional structures, such as hexagonal, honeycomb, open Kagome and quasicrystalline lattices. In addition, Soligno, Dijkstra & van Roij (2016) numerically investigated, by energy minimisation, the capillary deformations induced by adsorbed cubes at fluid-fluid interfaces for various Young's contact angles. In particular, they showed that strongly directional capillary interactions drive the cubes to self-assemble into hexagonal or graphene-like honeycomb lattices.

The notion of poles was also used in the theoretical studies of Kralchevsky & Denkov (2001), Danov *et al.* (2005) and Danov & Kralchevsky (2010), who theoretically predicted the meniscus shape around the particle under the assumption that it can be expanded into Fourier series. By integrating the linearised Young–Laplace equation along the midplane between the two particles and by using superposition, they derived a general integral expression for the capillary force and interaction energy between capillary multipoles of arbitrary orders.

A number of studies focused on the case of semi-submerged cylinders resting at the liquid interface. Janssens, Chaurasia & Fried (2017) introduced a study utilising the Young–Laplace equation to explore the configuration of the liquid–gas interface surrounding a floating particle. They examined the forces and torques on a partially submerged circular cylinder, considering surface tension disparities. Zhang, Zhou & Zhu (2018) evaluated how surface tension influences both the vertical and rotational stability of floating cylinders with differing cross-sectional shapes by altering the surface's curvature radius. Their research concluded that a diminished radius of curvature enhances rotational stability. Tan, Zhang & Zhou (2022) applied bifurcation theory to analyse the stability of multiple menisci formed in small concave arcs of cylinders. Additionally, Zhang & Zhou (2023) combined the Young–Laplace equation and bifurcation theory to study the stability of a floating cylinder situated between two parallel vertical plates and partly immersed in a liquid bath. Zhang *et al.* (2023) developed a novel methodology to forecast the stability of floating objects of any shape, anchored on the contact angle and geometrical features at the contact point, including object concavity and convexity.

The motivation for this study is to provide a solution to the Young-Laplace equation with varying boundary height for non-circular boundaries, assuming pinned conditions at the boundary, and to evaluate the correlation between this theoretical solution and experimental data. Although domain perturbation is a well-established asymptotic technique for solving differential equations in general domains, it has not previously

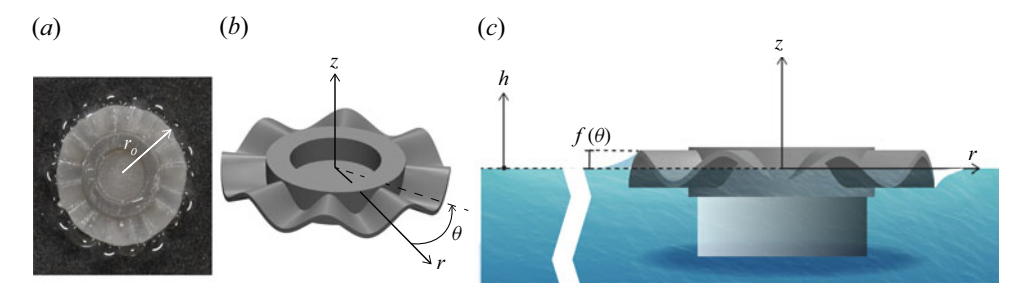


Figure 1. (a) A 3D printed particle held at the liquid–gas interface, where the outer particle's height is prescribed by $0.5 \sin(8\theta)$ mm. (b) A sketch of the rotated particle and (c) a side view of a particle which is held fixed on a liquid, where the height of its boundary is prescribed by $f(\theta)$.

been applied to the particle—liquid configurations examined here. To the best of our knowledge, all previous works have utilised multipoles as a solution method. Furthermore, while the assumption of pinned conditions at particle edges simplifies the theoretical analysis, experimental validation of this boundary condition remains uncertain. The complexity is further amplified for non-circular geometries, where significant deviations from circularity could render first-order solutions inadequate. This study demonstrates that, for weakly non-circular geometries, the domain perturbation technique is effectively applicable and yields good agreement with experimental results, confirming its efficacy as a versatile theoretical tool. However, for geometries with larger deviations from circularity, higher-order terms become necessary to accurately capture the observed behaviours.

The insights gained from these findings are vital to advancing our understanding of the collective behaviour and aggregation dynamics of multiple anisotropic floating particles and can be used to explain how different particle shapes affect their aggregation processes. In § 2, we present our solution, which employs the domain perturbation methodology, as well as the leading- and first-order solutions for the liquid-gas interface for a general particle shape. Then, in § 3, we discuss our experimental procedure and our methodology for analysing the data. Section 4, provides a comparison between the experimentally obtained liquid-gas interface and the analytical results for a set of anisotropic particle shapes. We conclude our findings in § 5. Appendix A provides additional details of the derivation of the leading- and first-order solutions for the second-order partial differential equation describing the interface shape. In Appendix B we express the solution in the dimensional form. Appendix C contains expressions for the deviations of equilateral polygons from circular arcs of the auxiliary circle in several specific cases. Finally, Appendix D discusses the error estimation in contact inclination angle at the particle boundary due to the liquid height uncertainty and Appendix E provides the formula for the second-order term in the asymptotic expansion of the height of the liquid-gas interface.

2. Analysis

We examine the steady-state interfacial deformations induced by anisotropic particles held at the liquid–gas interface. By applying domain perturbations, we formulate a general solution for the height of the liquid–gas interface that is pinned to the circumference of anisotropic particles. The assumption of pinned boundary conditions was explicitly used in several studies concentrating on particles with pinned contact lines, e.g. Yao *et al.* (2013, 2015) and Prakash, Perrin & Botto (2024). While the assumption of the pinned boundary condition is reasonable, it is typically taken as granted. As described below, our study shows that pinned boundary conditions provide good agreement with

experimental measurements even for non-circular particles with sinusoidal boundary conditions.

Consider a particle on top of a liquid where the particle consists of a hollow cylinder attached to a thin surrounding surface, as seen in figure 1(a). A cylindrical coordinate system (r, θ, z) , as depicted in figure 1(b) is adopted, where the origin $(r, \theta) = (0, 0)$ is located at the particle's centre and where z = 0 is the liquid height sufficiently far from the particle, as shown in figure 1(c). We denote the outer radius of the circular particle by r_o . In the case of non-circular particles, r_o represents the radius of the auxiliary circle inscribed in the particle's boundary circumference. Additionally, $d_r(\theta) \ge 0$ denotes the deviation of the outer circumference of the boundary from the circular arc of the inscribed circle with radius r_o . We also assume that the thickness of the surface along the circumference boundary is very small relative to the thickness of the particle. Thus, we can use the pinned boundary conditions along the rim of the particle. Accordingly, the rim of the models that we fabricated for the experiments was kept as thin as possible (see § 3).

We denote the height of the liquid–gas interface above z=0 outside of the particle as $h(r,\theta)$. Here, we shall find an asymptotic approximation for $h(r,\theta)$ in the domain $(r,\theta) \in (r_0+d_r(\theta),\infty)\times [0,2\pi)$, while accounting for various particle rim boundary shapes. For $\theta\in [0,2\pi)$ the outer boundary of the particle is determined by the functions $d_r(\theta)$ and $f(\theta)$, where $f(\theta)$ denotes the particle's height at the contact with the liquid–gas interface. Both these functions determine the shape of the interface and will serve in defining the boundary conditions for our problem.

The interface geometry is described by the Young-Laplace equation (Landau & Lifshitz 1987), $\Delta p = 2\gamma \kappa$, where κ denotes the mean curvature of the surface, $\Delta p = p_a - p(h)$, γ is the surface tension of the liquid, p_a is the atmospheric pressure and p(h) denotes the pressure acting on the liquid-gas interface $p(h(r,\theta)) = p_a - \rho g h(r,\theta)$, with ρ and g denoting the fluid density and gravitational constants, respectively. For a surface $(r,\theta,h(r,\theta))$ it is well known (see e.g. Kralchevsky & Nagayama 1994; Rotman 2009) that the mean curvature is given by $\kappa = 0.5\nabla \cdot [\nabla h/\sqrt{1+(\nabla h)^2}]$. Under the assumption that $h(r,\theta)$ is sufficiently small $(|h(r,\theta)| \ll 1)$ and with bounded derivatives, the Young-Laplace equation can be linearised yielding that $\gamma \Delta h = \Delta p$, which may be expressed in polar coordinates as

$$\gamma \left(\frac{1}{r^2} \frac{\partial^2 h}{\partial \theta^2} + \frac{1}{r} \frac{\partial h}{\partial r} + \frac{\partial^2 h}{\partial r^2} \right) = \rho g h(r, \theta). \tag{2.1}$$

Using the aforementioned definitions we can write the boundary conditions for our problem as

$$h|_{r=r_o+d_r(\theta)} = f(\theta), \tag{2.2}$$

where, for simplicity, we assume that $f(\theta)$ is a 2π periodic function and is sufficiently regular so it is possible to expand it into Fourier series in $\theta \in (0, 2\pi)$, namely $f(\theta) = w_0/2 + \sum_{n=1}^{\infty} (q_n \sin{(n\theta)} + w_n \cos{(n\theta)})$, where q_n and w_n denote the Fourier coefficients.

First, we render the problem dimensionless, by defining the following transformations:

$$H = \frac{h}{h_c}, \quad R = \frac{r}{r_o}, \quad D_r = \frac{d_r}{\varepsilon r_o}, \quad Q_n = \frac{q_n}{h_c}, \quad W_n = \frac{w_n}{h_c}, \quad n = 0, 1, \dots,$$
 (2.3)

where we assume that the maximal deviation of the circumference of the outer particle's boundary relative to the inscribed circle is sufficiently small, namely $\varepsilon := \max_{\theta \in [0,2\pi)} (|d_r(\theta)|/r_o)$ satisfies $0 < \varepsilon \ll 1$. Note that $h_c \neq 0$ denotes the characteristic liquid–gas interface height, whose value is unimportant, since both the equation and the

boundary conditions are linear and thus h_c cancels out. Moreover, note that the definition of r_o as the radius of the inscribed circle implies that we solve the dimensionless problem in the domain R > 1. As we shall show in the continuation of this section, our solution involves infinite series which contain Bessel functions, and thus the requirement that R > 1 is necessary to ensure convergence of the corresponding series.

Substituting the transformations in (2.3) into (2.1)–(2.2), we get that the dimensionless version of the problem is given by

$$\frac{\partial^2 H}{\partial \theta^2} + R \left(\frac{\partial H}{\partial R} + R \frac{\partial^2 H}{\partial R^2} \right) - B_o R^2 H = 0, \tag{2.4a}$$

$$H\big|_{R=1+\varepsilon D_r(\theta)} = \frac{W_0}{2} + \sum_{n=1}^{\infty} \left(W_n \cos\left(n\theta\right) + Q_n \sin\left(n\theta\right) \right), \tag{2.4b}$$

$$H\big|_{R\to\infty} = 0, (2.4c)$$

where $B_o = gr_o^2(\rho_L - \rho_G)/\gamma$ is the Bond number, which reflects the ratio of the gravitational force to the surface tension force. The Bond number typically appears in the analysis of interfacial phenomena such as of bubbles and drops (de Gennes, Brochard-Wyart & Quere 2003). Here, ρ_L denotes the liquid density and ρ_G denotes the gas density, where the underlying assumption is that $\rho_G \ll \rho_L$, thus we define $\rho_L - \rho_G = \rho$.

Note that the application of the boundary conditions at the particle's boundary given in (2.4b) to obtain a closed-form analytic solution is not straightforward in a general case since the shape of particle's boundary may be rather complicated. To overcome this problem, we use the domain perturbations method (Leal 2007) which provides an approximate mean to solve this problem under the assumption that $0 < \varepsilon \ll 1$, allowing us to replace the exact boundary condition with an approximate boundary condition that is asymptotically equivalent for $0 < \varepsilon \ll 1$, but applied at the boundary R = 1.

Note that by the definition of ε it follows that $|D_r(\theta)| \le 1$. Hence, we may expand $H|_{R=1+\varepsilon D_r(\theta)}$ into a Taylor series in ε around $\varepsilon = 0$, as follows:

$$H\big|_{R=1+\varepsilon D_r(\theta)} = H\big|_{R=1} + \varepsilon D_r(\theta) \frac{\partial H}{\partial R}\Big|_{R=1} + O(\varepsilon^2). \tag{2.5}$$

Moreover, expanding H in regular asymptotic series in ε , namely

$$H(R,\theta) = H_0(R,\theta) + \varepsilon H_1(R,\theta) + O(\varepsilon^2), \tag{2.6}$$

and using these expansions in (2.4), we get that the leading-order problem with respect to ε is given by

$$R^2 \frac{\partial^2 H_0}{\partial R^2} + R \frac{\partial H_0}{\partial R} + \frac{\partial^2 H_0}{\partial \theta^2} - B_o R^2 H_0 = 0, \tag{2.7a}$$

$$H_0\big|_{R=1} = \frac{W_0}{2} + \sum_{n=1}^{\infty} (W_n \cos(n\theta) + Q_n \sin(n\theta)),$$
 (2.7b)

$$H_0\big|_{R\to\infty} = 0. (2.7c)$$

Using separation of variables, we obtain that the general solution to the problem in (2.7) is given by

$$H_0(R,\theta) = \frac{K_0(\sqrt{B_o}R)A_0}{2} + \sum_{n=1}^{\infty} K_n(\sqrt{B_o}R) \left[A_n \cos(n\theta) + B_n \sin(n\theta) \right], \quad (2.8)$$

where K_n , n = 0, 1, 2, ..., denotes the modified Bessel function of the second kind (Olver *et al.* 2010) and A_n , B_n are constants which are determined by using the boundary conditions in (2.7b), namely

$$A_n = \frac{W_n}{K_n(\sqrt{B_o})}$$
 and $B_n = \frac{Q_n}{K_n(\sqrt{B_o})}$. (2.9)

Next, similarly to the discussion above, we get at the first, $O(\varepsilon)$, order the following problem:

$$R^{2} \frac{\partial^{2} H_{1}}{\partial R^{2}} + R \frac{\partial H_{1}}{\partial R} + \frac{\partial^{2} H_{1}}{\partial \theta^{2}} - B_{o} R^{2} H_{1} = 0,$$

$$H_{1} \Big|_{R=1} = -D_{r}(\theta) \frac{\partial H_{0}}{\partial R} \Big|_{R=1},$$

$$H_{1} \Big|_{R \to \infty} = 0.$$
(2.10)

Using again the separation of variables and the solution for H_0 given in (2.8), we obtain that the first-order solution is given by

$$H_1(R,\theta) = \frac{K_0(\sqrt{B_o}R)\tilde{A}_0}{2} + \sum_{n=1}^{\infty} K_n(\sqrt{B_o}R)[\tilde{A}_n\cos(n\theta) + \tilde{B}_n\sin(n\theta)], \quad (2.11)$$

where the constants \tilde{A}_n and \tilde{B}_n , which are determined by using the boundary conditions in (2.10), are given by

$$\tilde{A}_{n} = \frac{\sqrt{B_{o}}}{2\pi K_{n}(\sqrt{B_{o}})} \int_{0}^{2\pi} G(\theta) \cos(n\theta) d\theta, \quad n = 0, 1, 2, \dots,$$

$$\tilde{B}_{n} = \frac{\sqrt{B_{o}}}{2\pi K_{n}(\sqrt{B_{o}})} \int_{0}^{2\pi} G(\theta) \sin(n\theta) d\theta, \quad n = 1, 2, \dots,$$
(2.12)

where for brevity we use the following notation:

$$G(\theta) = D_r(\theta) \left\{ \frac{\left(K_{-1}(\sqrt{B_o}) + K_1(\sqrt{B_o})\right) A_0}{2} + \sum_{m=1}^{\infty} \left(K_{m-1}(\sqrt{B_o}) + K_{m+1}(\sqrt{B_o})\right) \left[A_m \cos(m\theta) + B_m \sin(m\theta)\right] \right\}.$$

$$(2.13)$$

Thus, we obtained an approximate solution for the liquid–gas interface height outside of a particle held at the liquid–gas interface with a non-circular shape and anisotropic height at the pinned contact line. The dimensionless solution is provided by $H(R,\theta)=H_0(R,\theta)+\varepsilon H_1(R,\theta)$, where the leading- and first-order terms $H_0(R,\theta)$ and $H_1(R,\theta)$ are given in (2.8)–(2.9) and (2.11)–(2.13), respectively. Note that, by our construction, the solution is valid for R>1, which follows from defining r_o as the radius of the inscribed circle. The reason for this choice is the convergence issues. It is known (Olver *et al.* (2010), see formula 10.30.2) that $K_{\nu}(R) \to \Gamma(\nu)/(2(R/2)^{\nu})$ when $\nu \neq 0$, $R \to 0$. Therefore, the sum $\sum_{\nu=1}^{\infty} K_{\nu}(\sqrt{B_o}R)/K_{\nu}(\sqrt{B_o})$ is not convergent for |R|<1. On the other hand (Olver *et al.* 2010, see formula 10.25.3), $K_{\nu}(R) \sim (\pi/2R)^{1/2}e^{-R}$ for $R \to \infty$ and fixed ν , so that $\sum_{\nu=1}^{\infty} K_{\nu}(\sqrt{B_o}R)/K_{\nu}(\sqrt{B_o})$ converges for |R|>1. Thus, defining r_o as the radius of the inscribed circle, we obtain that the dimensionless radius satisfies R>1, so that our solution is indeed convergent.

The dimensional form of the solution is given in Appendix B.

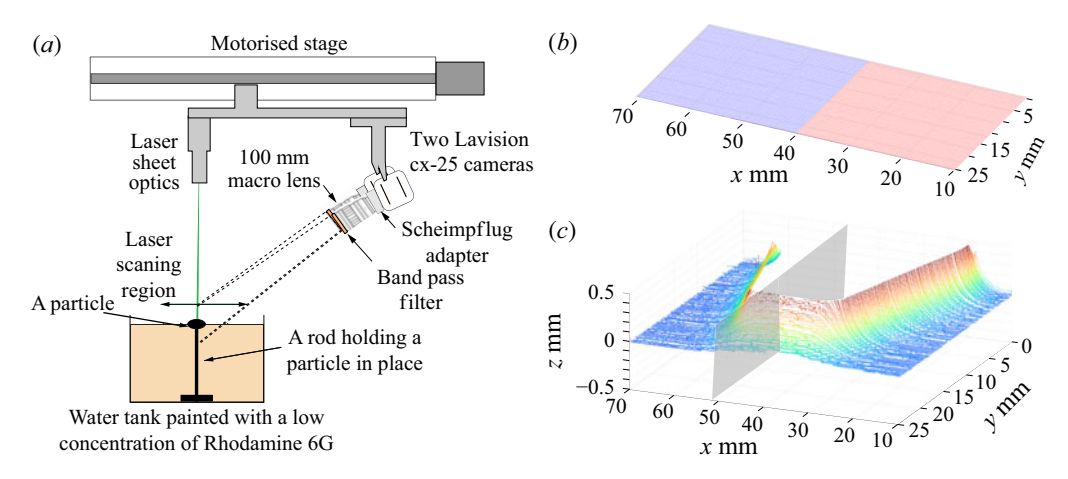


Figure 2. (a) The experimental set-up. The particles are held at the water-air interface, where the water is painted with a low concentration of Rhodamine 6G. A Nd: Yag 532 nm laser is used to excite the Rhodamine 6G, causing it to fluoresce at a wavelength of 550 nm. An optical set-up is used to form a thin laser sheet (\sim 0.1 mm) that illuminates a cross-section of the water's interface across the particle. The images were acquired by a camera with a band-pass filter attached to its lens, with a cutoff wavelength of 550 nm. (b) A raw scan of the free surface without any model present. The figure also indicates the regions captured by each camera: red indicates the area recorded by camera 1, and blue corresponds to camera 2. The standard deviation of the free-surface measurements is 0.02 mm, although this variation is too small to be discernible in the figure. (c) A raw scan result obtained for a flat hexagon, which is placed 0.5 mm higher than the air–liquid interface. The displacement is magnified by a factor of 10 for visual representation. These results are obtained by a camera which is placed at an angle of 30° in relation to the central plane, marked in grey, and at an angle of 10° to the horizon. The far side of the model was captured by the second camera.

3. Experiments

Measuring relatively large surface deformations on a transparent fluid surface poses unique experimental challenges. While interferometric techniques offer high accuracy for very small surface deformations, they are generally unsuitable for large-amplitude measurements. This limitation arises because interferometry relies on precise optical phase differences, and large height variations typically exceed the coherence length of conventional interferometric set-ups, leading to ambiguity and loss of measurable interference fringes (Hinsch 1978). Alternative techniques such as structured-light profilometry or standard optical three-dimensional scanning methods depend on a diffusely reflecting, opaque surface to reconstruct three-dimensional profiles accurately. Consequently, their application is severely limited by the transparent and reflective nature of water surfaces, resulting in unreliable or non-existent signal detection (Zhang 2018). Due to these constraints, the present study utilised a fluorescence-based laser sheet scanning approach combined with stereo imaging, enabling accurate measurement of significant liquid surface elevations around particles held at the liquid–gas interface without the aforementioned limitations.

A schematic representation of the experimental set-up is shown in figure 2(a). The setup was developed to quantitatively measure the liquid surface elevation around particles placed at the free water surface, using a laser sheet scanning method combined with stereo imaging from two high-resolution cameras (LaVision CX-25). The measured surface elevations were subsequently compared with the theoretical asymptotic solution. Particles used in the experiment were fabricated using a Formlabs Form 3 stereolithography (SLA) 3D printer utilising Formlabs' Tough 1500 UV-cured resin. Each particle featured a thick, stable base and a thin peripheral rim, specifically designed to minimise geometric

distortions caused by resin shrinkage during printing and the curing processes. After complete UV curing, the particles underwent visual inspection and manual dimensional verification to confirm conformity with the intended design. Although precise deviations were not systematically quantified, no significant discrepancies were detected. Given Formlabs' documented high-resolution capabilities and extensive prior experience with the Form 3 printer, we considered the fabricated geometries sufficiently accurate for the purposes of this study. Each particle was carefully placed onto the free water surface using a rigid supporting base rod to eliminate any motion during measurements, thus ensuring the best possible reconstruction quality. The tank was filled with purified water doped with a dilute concentration of Rhodamine 6G fluorescent dye. Although the water level was adjusted carefully, experimental constraints limited precise control to within ± 0.05 mm of the desired water height. The analytical solution assumes that the far-field liquid level is zero. Hence, considering this uncertainty will introduce an effective deviation to the relative height of the model edge, where the fluid is pinned. The uncertainty in the water level will effectively introduce a change to inclination angle of the meniscus close to the contact line. Appendix D presents a derivation of the inclination angle and examines the effects of the water level uncertainty in the experiments. It shows that the maximum uncertainty of ± 0.05 mm in the measurement of the liquid–gas interface at far field results in the error of the order of $\pm 1\%$ in the inclination angle of the meniscus. Because the solution is decaying to the flat surface boundary, the maximal error in the solution is bounded by the measurement uncertainty applied to the boundary. In addition, analysis of the measurement presented in figure 2(b) shows that overall shape of the measured surface is correct, i.e. flat in this case. Consequently, it is reasonable to assume that the main findings and comparisons are mostly unaffected by this relatively small experimental limitation. A Nd:YAG laser (Quantel Evergreen-200), emitting at a wavelength of 532 nm, was utilised to excite the Rhodamine dye, resulting in fluorescent emission at approximately 550 nm. The laser beam was transformed into a thin laser sheet (\sim 0.1 mm thickness) using a cylindrical lens, illuminating a vertical cross-section of the water's surface around the particle. Fluorescent emissions were recorded using two highresolution LaVision CX-25 cameras, each equipped with a 100 mm macro lens achieving a magnification of 54.3 (pixels mm⁻¹). To enhance image quality and signal-to-noise ratio, each camera lens was fitted with a 550 nm long-pass optical filter (Edmund Optics #84-757), effectively eliminating scattered laser light and isolating the dye fluorescence. Cameras were symmetrically positioned $\pm 30^{\circ}$ horizontally from the particle's central axis and inclined at approximately 10° above the horizontal plane. This dual-camera configuration significantly reduced shadowing artefacts caused by elevated portions of the particle rim, thereby ensuring clear visualisation of the illuminated intersection line on the water's surface. The laser sheet and both cameras were mounted on a precision motorised translation stage, enabling incremental spatial scanning in steps of 0.1 mm across the particle with a positional accuracy of approximately 0.001 mm. To maintain sharp imaging throughout the scan, each camera employed a Scheimpflug adapter to compensate effectively for focal-depth variations occurring during stage translation. As the cameras were placed on one side of the tank, only the front-facing half of the particle was captured. The recorded images were analysed using an in-house image processing algorithm designed to extract surface elevation profiles from each cross-sectional image. These profiles were then compiled to reconstruct a detailed three-dimensional representation of the water surface surrounding the particle. To validate the reconstruction accuracy, we performed repeated scans of the undisturbed free surface in the absence of any model. An example of such a scan is shown in figure 2(b). Across the scanned region and between both cameras (each camera scan region is marked by a different colour), the standard deviation in the measured

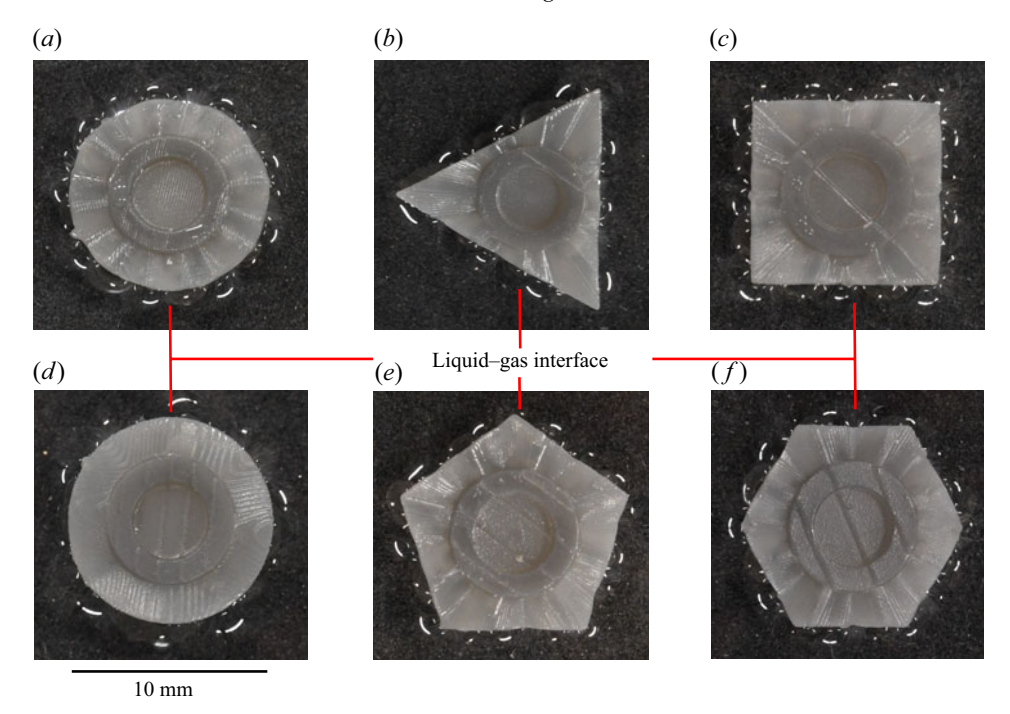


Figure 3. The 3D printed particles made of Tough 1500 V1, with a reference auxiliary diameter circle of 10 mm held at the liquid–gas interface. The outer particles' height is prescribed by $0.5 \sin(8\theta)$ mm for (a) circle, (b) triangle, (c) square, (e) pentagon, (f) hexagon and by $0.5 \sin(4\theta)$ mm for (d) circle.

surface height was found to be approximately 0.02 mm. This value is significantly smaller than the typical interface deformations observed in our experiments, and thus confirms that the measurement system provides sufficient precision for reliable comparison with the theoretical predictions. An illustrative example of the reconstructed water surface is shown in figure 2(c), where the elevation scale has been amplified by a factor of ten for improved visualisation. Prior to analysis, the mean far-field water level was subtracted from the measurements, establishing the undisturbed free-surface reference at zero elevation. While there are occasionally small regions which cannot be detected in the raw images due to light reflections or some impurities at the water's surface, leading to small void regions in the experiments, the technique has proven reliable and the results are reproducible. To ensure that the measurement system performs well we quantified the standard deviation of the measured water surface elevation in the undisturbed far-field region away from the particle model, which consistently yielded an estimated precision of approximately 0.02 mm.

Figure 3 shows a series of SLA 3D-printed particles held at the liquid–gas interface, each featuring a central reference circle of 10 mm diameter. The images illustrate various particle geometries: (a,d) circles, (b) triangle, (c) square, (e) pentagon and (f) hexagon. The outer edges of the particles incorporate sinusoidal undulations defined by amplitudes of $0.5 \sin(8\theta)$ mm for the polygonal shapes (b,c,e,f) and $0.5 \sin(4\theta)$ mm for the circular shape shown in (d). Off-axis illumination was employed to enhance visualisation of the particle surface features and the associated deformation of the liquid–gas interface around the rims. The visible interface distortions around each particle highlight the interplay between particle geometry and surface tension effects, emphasising both the fidelity achievable through SLA printing and the subtle liquid interface deformation investigated in this study.

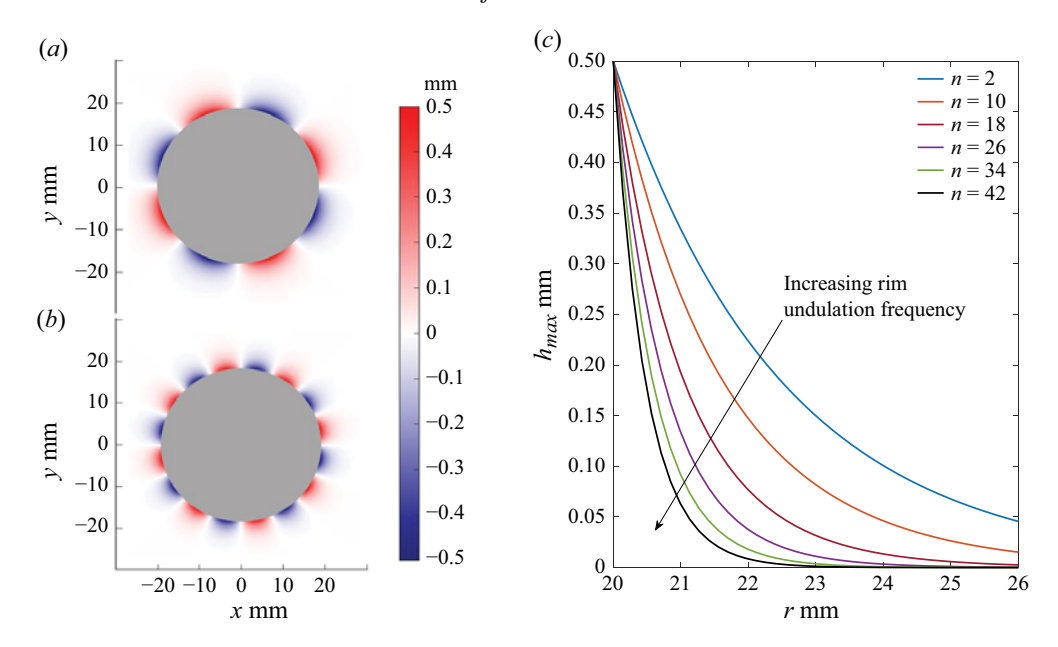


Figure 4. Analytical results for the liquid–gas interface for particles placed by held at the liquid–gas interface with $r_0 = 20$ mm, where the outer particles' height is prescribed by: (a) $0.5 \sin(4\theta)$ mm and (b) $0.5 \sin(8\theta)$ mm. (c) Maximum heights (at any r) of the liquid–gas interfaces versus r obtained by solving the Young–Laplace equation with different boundary conditions, given by $h|_{r=20} = 0.5 \sin(n\theta)$ mm, where the uppermost and the lowermost curves correspond to n=2 and n=42, respectively.

4. Results

This section presents results obtained for two cases, circular and non-circular particles, as well as a comparison between the theoretical and experimental results. In the case of the circular boundary of the particle, the solution to the Young-Laplace equation is obtained analytically. However, in the case of a non-circular boundary, we use the domain perturbation technique, which yields an asymptotic solution to the Young-Laplace equation. This asymptotic solution depends on the difference in absolute value between the circular and the perturbed boundary. For all results presented in this section, except § 4.4, we employ the sum of the leading- and the first-order terms in the asymptotic expansion of $H(R,\theta)$, namely $H(R,\theta) \approx H_0(R,\theta) + \varepsilon H_1(R,\theta)$, where both, $H_0(R,\theta)$ and $H_1(R,\theta)$, contain 20 modes in the Fourier series. In § 4.4, we show an example of convergence relative to the number of terms in the asymptotic expansion. This is achieved by comparing the results obtained using $H^{(0)}(R,\theta) = H_0(R,\theta)$, $H^{(1)}(R,\theta) = H_0(R,\theta) + \varepsilon H_1(R,\theta)$ and $H^{(2)}(R,\theta) = H_0(R,\theta) + \varepsilon H_1(R,\theta) + \varepsilon^2 H_2(R,\theta)$, where $H_0(R,\theta)$, $H_1(R,\theta)$ and $H_2(R,\theta)$ contain 20 modes in the Fourier series. Note that the expressions for $H_0(R,\theta)$ and $H_1(R,\theta)$ are given in § 2 and the expression for $H_2(R,\theta)$ is derived in Appendix E. Convergence details relative to the number of modes are given in figure 9 in Appendix A.

4.1. Analytic results for circular particles

Figure 4(a,b) shows two examples of the liquid–gas interface obtained by using the solution given in (2.8), calculated for a circular particle with sinusoidal boundary conditions. As expected according to the boundary conditions, the interface is sinusoidal in the rotating angle θ along the particle's boundary, and it is flat and vanishing far enough away from the particle. This is reasonable since the Bessel functions appearing in the

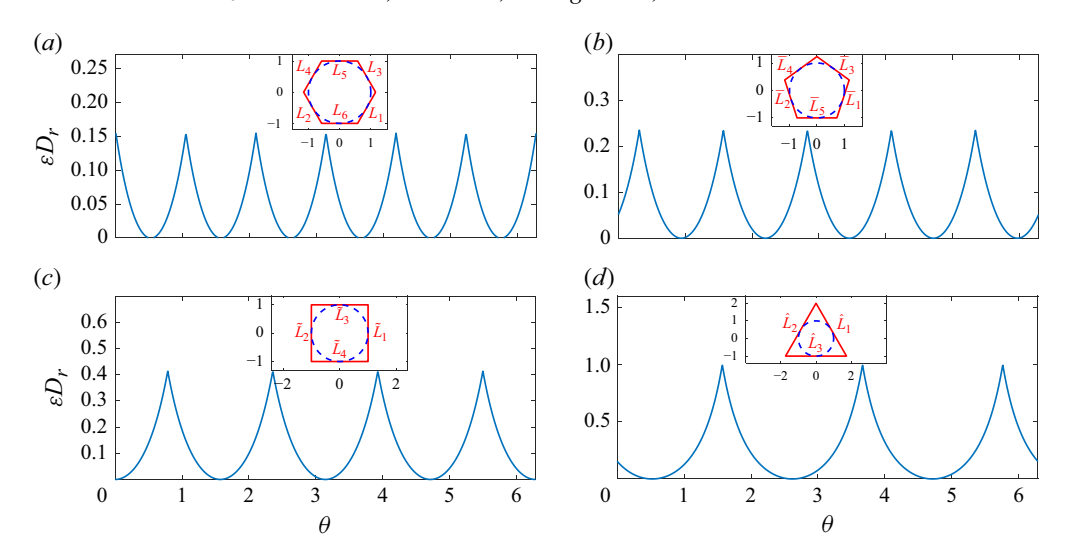


Figure 5. The perturbation functions $\varepsilon D_r(\theta)$ relative to the unit circle for (a) a hexagon, (b) a pentagon, (c) a square and (d) a triangle. The sketches of the corresponding circumferences of the particles in our experiments and in the asymptotic solutions are shown in the insets.

leading-order solution, which is exact in the case of the circular particle, are decreasing functions of r. The boundary conditions of figures 4(a) and 4(b) have a proportional value to $\sin(4\theta)$ and $\sin(8\theta)$ mm, respectively. Based on these figures, when the frequency of the sinusoidal wave increases, not only does the density of the peaks increase, but they also vanish at a faster rate as r increases towards the far boundary. The dependency of the influence of the particle's distance on its rim undulation frequency is further emphasised in figure 4(c), where we show the maximal liquid—gas interface height (at any r) versus r for different frequencies of the sinusoidal wave prescribed along the outer boundary of the particle. According to figure 4(c), as the rim undulation frequency increases the liquid—gas interface flattens closer to the particle.

4.2. Asymptotic results for non-circular particles

Here, we show the liquid–gas interfaces for the following particle's shapes: equilateral hexagon, pentagon, square and triangle. As presented in the insets in figure 5, we define an auxiliary inscribed circle and scale the problem by using its radius r_o . To obtain the asymptotic solution by using the domain perturbation technique, we refer to the circumferences of these shapes as to a small deviation $\varepsilon D_r(\theta)$ from a circle. Note that as the sides number of an equilateral particle decreases, the deviation from the circle increases. Figure 5 illustrates, however, that the largest deviation between the studied shapes, which is equal to one, occurs at the corners of the triangle. As a result, our method becomes inapplicable, regardless of the number of terms in the asymptotic expansion, at the vicinity of the triangle's corners only.

More specifically, for each θ , $\varepsilon D_r(\theta)$ denotes the distance between the corresponding shape and the inscribed circle, expressed in radial coordinates. The graphs of $\varepsilon D_r(\theta)$, are shown in figure 5 and the corresponding expressions for $\varepsilon D_r(\theta)$ are given in Appendix C. As expected, the maximum of $\varepsilon D_r(\theta)$ increases as we move from a hexagon to a pentagon, from a pentagon to a square and from a square to a triangle, which reflects the fact that the circumference of the hexagon is the closest (among the discussed shapes) to those of

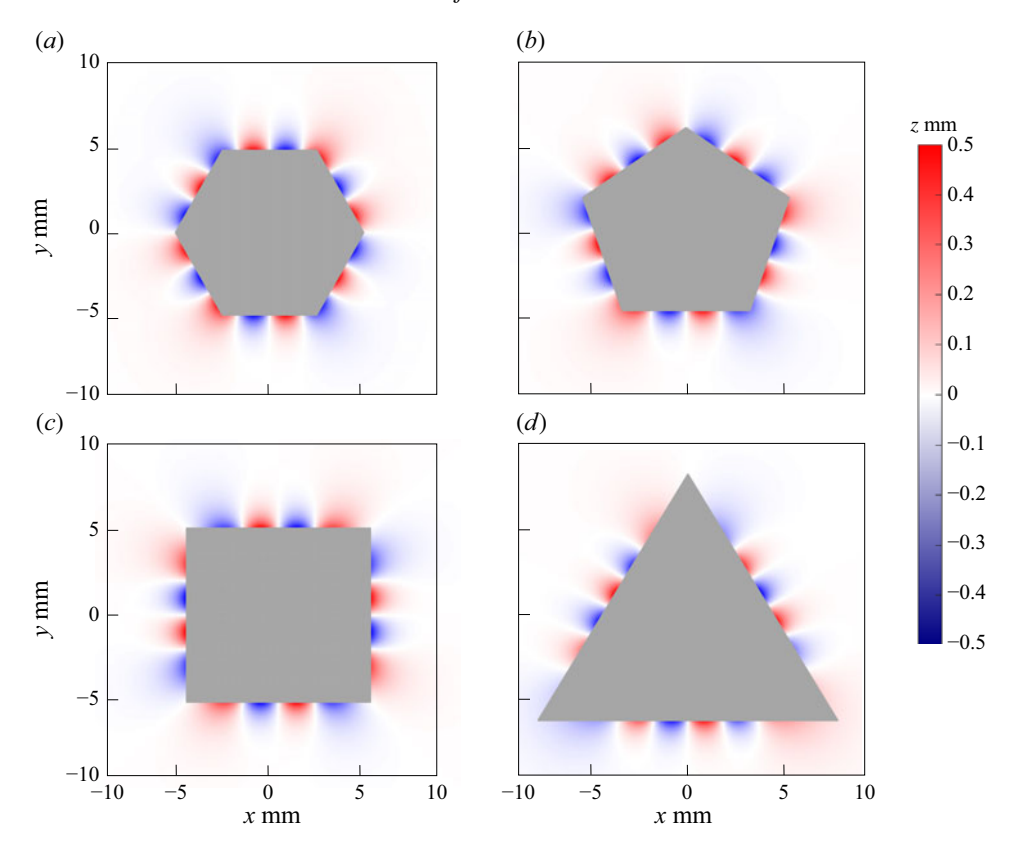


Figure 6. The liquid–gas interface obtained by the asymptotic solution for (a) hexagonal, (b) pentagonal (c) square and (d) triangular particles, whose outer heights are prescribed by $0.5 \sin(8\theta)$ mm and where $r_0 = 5$ mm in all cases.

the inscribed circle and the circumference of the triangle is the furthest from those of the inscribed circle.

Figure 6 presents results for the liquid–gas interface obtained using the asymptotic solution given in (2.6) including both the leading- and first-order solutions prescribed in (2.8) and (2.11), respectively. The asymptotic results were calculated for equilateral hexagonal, pentagonal, square and triangular particles with sinusoidal boundary conditions. The liquid-gas interface is pinned to the particle, and hence its boundary conditions are determined according to the particle's boundary outer height. As the particle circumference approaches the circle, the liquid-gas interface near the particle's boundary approaches the sinusoidal wave (for a given r, as a function of θ), as the asymptotic approximation becomes more accurate. As we move along the particle's boundaries towards the corners, where the deviation from a circle is maximal, the amplitude of the sinusoidal-like wave decreases, since the asymptotic approximation is less accurate there. When $0 < \varepsilon < 1$, this inaccuracy may be improved by adding additional terms of higher orders to the asymptotic expansion in (2.6), (for an additional discussion, see § 4.4). Moreover, similar to the circular particles, the maximal height (in absolute value) of the liquid-gas interface decreases along the radial direction as we move from the particle's boundary until the interface flattens.

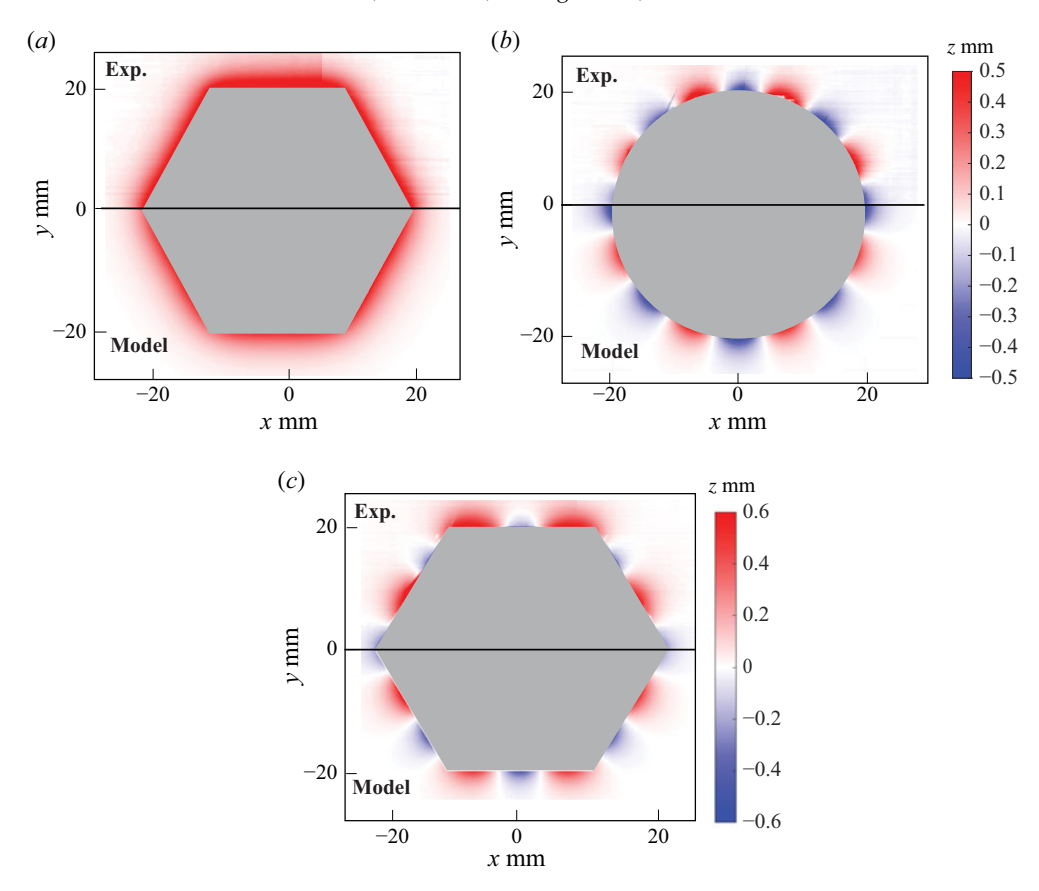


Figure 7. A comparison between experimental (upper half of the panels a–c) and theoretical (lower half of the panels a–c) results for the liquid–gas interface in three cases: (a) a hexagonal particle held at the liquid–gas interface at the height of 0.5 mm, (b) a circular particle with the outer height of 0.5 sin (8θ) mm and (c) a hexagonal particle with the outer height of $0.1 + 0.5 \sin(8\theta)$ mm. In all panels the radius of the inscribed circle is $r_0 = 20$ mm and the height of the particles is relative to the liquid–gas interface sufficiently far from the particle. The colour bar refers to both cases (experimental and theoretical) for all panels.

4.3. Comparison between theoretical and experimental results

In figure 7 we show a comparison between experimental (upper half of all panels) and theoretical (lower half of all panels) results for the liquid–gas interfaces for the following particle shapes: an equilateral flat hexagonal particle which is above the liquid level by 0.5 mm, a circular particle where the outer particle's height is prescribed by $0.5 \sin(8\theta)$ mm and an equilateral hexagonal particle where the outer particle's height is prescribed by $0.1 + 0.5 \sin(8\theta)$ mm. The circumference radius of the inscribed circle is 20 mm for all particles. As can be seen, in all cases there is a quantitative agreement between theory and experiment, except probably in close vicinity of the hexagon's corners. This inaccuracy in theoretical results might be easily improved by taking into account more terms in the asymptotic expansion of $h(r, \theta)$, as discussed in § 4.4.

4.4. Limitations of the method

As mentioned in § 2, the asymptotic nature of the theoretical approach employed in this study implies the need to use small values of ε , $0 < \varepsilon \ll 1$. Moreover, note that the error of the asymptotic expansion $H^{(M)}(R, \theta) := \sum_{m=0}^{M} \varepsilon^m H_m$, where $M = 0, 1, 2, 3 \ldots$, is

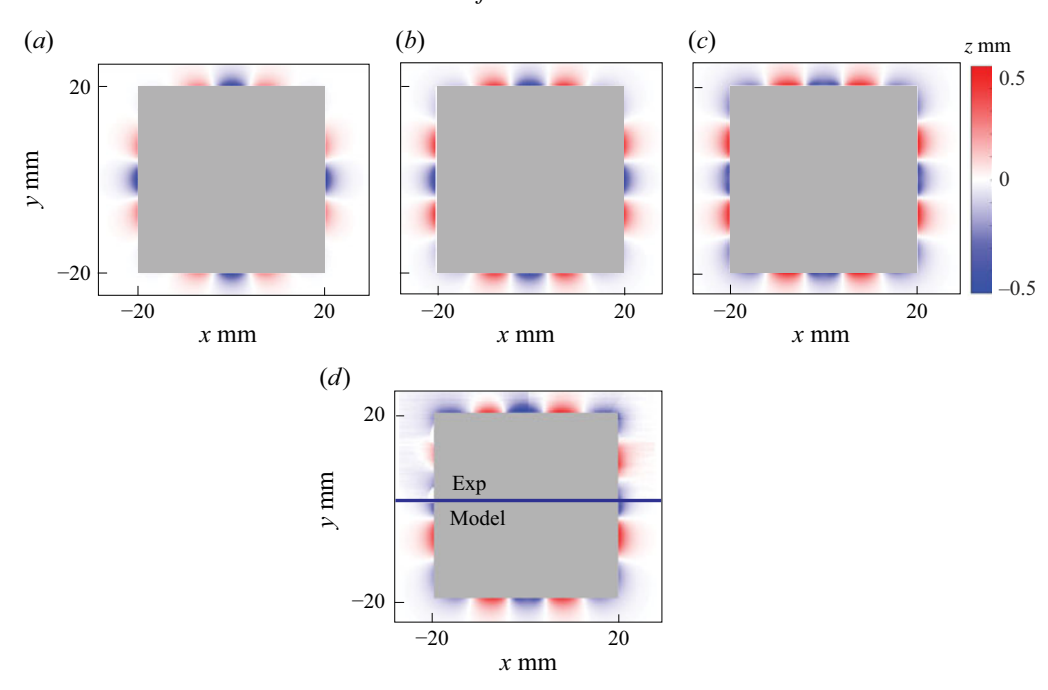


Figure 8. An example of the convergence analysis relative to the number of terms in the asymptotic expansion for a square-shaped particle with an outer height of 0.5 sin (8θ) mm using (a) only the leading-order term $H^{(0)}(R,\theta)$, (b) the sum of the leading- and the first-order terms $H^{(1)}(R,\theta)$, (c) the sum of the leading-, the first- and the second-order terms $H^{(2)}(R,\theta)$ and (d) a comparison between experiment (upper half of the panel) and $H^{(2)}(R,\theta)$ (lower half of the panel). In all panels the radius of the inscribed circle is $r_0 = 20$ mm.

of order $O(\varepsilon^{M+1})$, namely $(H(R,\theta) - H^{(M)}(R,\theta)) = O(\varepsilon^{M+1})$. Thus, as ε increases towards 1, we get a larger deviation of the asymptotic expansion $H^{(1)}(R,\theta)$ discussed above from $H(R,\theta)$, which implies that, in order to get satisfactory accuracy for relatively large $0 < \varepsilon < 1$, higher-order terms in the asymptotic expansion are required.

To illustrate the effects of the expansion order on the accuracy of the solution, we performed an experiment with a square-shaped particle, where the radius of the inscribed circle is 20 mm and the particle's outer height is given by 0.5 sin (8 θ) mm. It is easy to verify that, for a general square-shaped particle, $\varepsilon = 1/\cos{(\pi/4)} - 1 \approx 0.414$, which is visualised by the maximum values in figure 5(c). This value of ε is relatively large and, as shown in figure 8(a), results in a significant error in the leading-order term solution $H^{(0)}(R,\theta) = H_0(R,\theta)$ given in (2.8)–(2.9). As shown in figure 8(b), this error considerably decreases when taking into account the sum of the leading- and first-order terms $H^{(1)}(R,\theta) = H_0(R,\theta) + \varepsilon H_1(R,\theta)$, where $H_1(R,\theta)$ is given in (2.11)–(2.13). However, the decrease in error is not sufficient, since the solution $H^{(1)}(R,\theta)$ misses the correct behaviour near the corners of the square, where $\varepsilon D_r(\theta)$ is the largest and approaches 0.414. Thus, figure 8(c) depicts the solution $H^{(2)}(R,\theta)$, which takes into account the sum of three terms: the leading-, the first- and the second-order terms, where the expression for $H_2(R, \theta)$ is derived in Appendix E. Figure 8(d) visualises the agreement between the experimental measurement of the liquid-gas interface for a square-shaped particle (upper half of the panel) and the solution $H^{(2)}(R,\theta)$ (lower half of the panel). According to this figure, it is obvious that including additional terms in the asymptotic expansion significantly improves the accuracy of the solution, and in particular, taking 3 terms in the expansion allows us to get the correct behaviour along the sides of a square,

including its corners. Note that there is an excellent agreement between the asymptotic solution with 3 terms in the expansion and the experimental measurements.

In summary, figure 8 demonstrates that the theoretical method proposed in the current study can be applied to more complex geometries. However, if ε increases, additional orders in the asymptotic expansion are required. Specifically, while asymptotic solutions are typically employed for $0 < \varepsilon \ll 1$, here, we show that, by employing higher-order terms in the expansion, we may obtain satisfactory results even for a relatively large ε , $\varepsilon \approx 0.414$. Note that, for the hexagon shown in figure 7, the value of ε was relatively small, $\varepsilon \approx 0.15$, and hence even the solution $H^{(1)}(R,\theta)$ composed of the leading and first terms only agrees well with the experiments.

5. Conclusions

This study leverages the domain perturbation technique to analyse the liquid–gas interface deformation in the vicinity of an anisotropic particle held at the liquid–gas interface, where the liquid–gas interface is assumed to be pinned to the particle's edges. We obtain a closed-form solution for particles with non-circular complex shapes and varying contact-line heights. This technique provides an appealing method for non-circular domains, complementing previously used techniques, such as multipoles, which were implemented for circular or ellipsoidal particles (Kralchevsky & Denkov 2001; Danov *et al.* 2005; Danov & Kralchevsky 2010).

Our theoretical results were validated by experiments performed using high-resolution laser scanning that captured the deformation of the liquid-gas interface around 3D printed particles held at the liquid-gas interface. We tested circular, hexagonal and square-shaped particles with flat and sinusoidal rims which are placed at, or at a shifted height from, the liquid–gas interface. The overall comparison shown in figures 7 and 8 reveals that the surface shape around the particle and the consequent effects it has on its vicinity seem to be well correlated between experiments and theory. This provides us with confidence that the analysis method and the assumption of pinned boundary conditions employed in this study provide a good estimation of the effects of particles on the surrounding liquid-gas interface. Note that we decided to concentrate on polygonal shapes in order to highlight the robustness of our approach, which succeeds in yielding a good agreement between theory and experiment, even though polygons contain sharp edges, which generally may complicate the theoretical modelling. For the cases of polygons that have relatively large deviations from a circle, such as a square, taking into account additional terms in the asymptotic expansions is required to resolve the accuracy issues in the vicinity of the corners, as shown in figure 8.

Building on this work, future studies can generalise the present approach to systems of multiple floating anisotropic particles, enabling analysis of their collective capillary interactions and self-assembly dynamics. By combining the domain perturbation method with bipolar coordinate techniques, as discussed by Kralchevsky & Nagayama (2000), the model can be extended to derive explicit solutions for pairwise interface deformations and interaction forces induced by complex particle shapes. This will help to clarify how particle anisotropy and orientation dictate not only attractive or repulsive capillary forces but also significant capillary torques that can induce mutual rotations, an effect discussed by Koens *et al.* (2019), who highlighted the distinct roles of near-field and far-field effects in the self-assembly of magnetic capillary disks. Moreover, adopting superposition approximations similar to those employed by Singer (2004) and Beatus, Bar-Ziv & Tlusty (2012) could simplify the modelling complex particle self-assembly. Collectively, such advances will offer a more complete picture of anisotropic capillary interactions and

inform the design of self-assembled interfacial particle networks, paving the way toward programmable interfacial materials with tailored assembly properties (Poty *et al.* 2014).

Supplementary material. Supplementary material is available at https://doi.org/10.1017/jfm.2025.

Acknowledgements. J.T.J. is partially supported by a Technion Post-Doctoral fellowship. This work is partially supported by the Zuckerman STEM Leadership Program.

Declaration of interests. The authors report no conflict of interest.

Appendix A. Approximate solution of the problem in (2.4)

We begin by solving the leading-order problem given in (2.7). We assume that the solution may be obtained by separation of variables, namely that there exist two functions, $\mathcal{R}(R)$ and $\Theta(\theta)$, so that the solution of (2.7) may be expressed as $H_0(R,\theta) = \mathcal{R}(R)\Theta(\theta)$. Substituting this separation of variables into equation (2.7a) and employing standard mathematical manipulations, we obtain the following equation:

$$\frac{R^2}{\mathcal{R}}\frac{\partial^2 \mathcal{R}}{\partial R^2} + \frac{R}{\mathcal{R}}\frac{\partial \mathcal{R}}{\partial R} - B_o R^2 = -\frac{1}{\Theta}\frac{\partial^2 \Theta}{\partial \theta^2}.$$
 (A1)

Since the left-hand side of the equation in (A1) depends only on R and the right-hand side of this equation depends only on θ , there exists a constant λ , so that

$$\frac{R^2}{\mathcal{R}}\frac{\partial^2 \mathcal{R}}{\partial R^2} + \frac{R}{\mathcal{R}}\frac{\partial \mathcal{R}}{\partial R} - B_o R^2 = -\frac{1}{\Theta}\frac{\partial^2 \Theta}{\partial \theta^2} = \lambda. \tag{A2}$$

Considering the equation for Θ in (A2) and noting that, according to the boundary condition in (2.7b) $\Theta(\theta)$ is 2π periodic in θ , we may conclude that the eigenvalues λ are necessarily of the form $\lambda = n^2$, for $n = 0, 1, 2, \ldots$, and the corresponding eigenfunctions are given by

$$\Theta_n(\theta) = A_n \cos(n\theta) + B_n \sin(n\theta), \quad n = 0, 1, 2, \dots$$
 (A3)

Then, for these eigenvalues the resulting equations for R are given by

$$R^2 \frac{\partial^2 \mathcal{R}}{\partial R^2} + R \frac{\partial \mathcal{R}}{\partial R} - \left(B_o R^2 + n^2 \right) \mathcal{R} = 0, \quad n = 0, 1, 2, \dots$$
 (A4)

This type of equation is known as a modified Bessel equation and its solutions are called modified Bessel functions (Olver *et al.* 2010). Due to the fact that the modified Bessel function of the first kind, $I_n(R)$, is unbounded as R tends to infinity, and we seek a solution that satisfies (2.7c), we may only use the modified Bessel function of the second kind, $K_n(R)$ (which tends to 0 when $R \to \infty$). Hence, for the problem in (A4) we will use the eigenfunctions

$$\mathcal{R}(R) = K_n(\sqrt{B_o}R), \quad n = 0, 1, 2, \dots,$$
 (A5)

so that the general solution to the equation in (2.7a) is given by (2.8). Imposing on the solution in (2.8) the boundary conditions in (2.7b), we obtain that the constants A_n and B_n are as prescribed in (2.9).

Note that since the equation for H_1 as given in (2.10) is exactly of the same form as the equation for H_0 , by using the same procedure as described above, we get the same general solution for H_1 as for H_0 , see (2.11). Imposing the boundary conditions in (2.10) on the

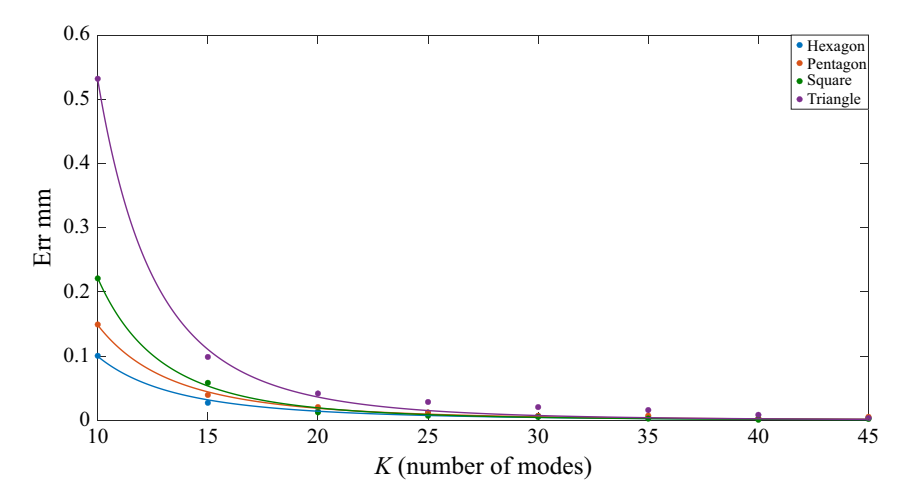


Figure 9. The error, Err defined in (A8), arising from the truncation of a finite number of modes in the Fourier series of the asymptotic solution $H(r, \theta)$ versus the number of modes, K. The full circles represent results obtained by simulation for the hexagon, pentagon, square and triangle, which correspond to the results shown in figure 6, and the curves, which were obtained by least square fitting to the simulation results, are to guide the eyes.

general solution for H_1 in (2.11) and substituting (2.8), we get that

$$\frac{K_0(\sqrt{B_o})\tilde{A}_0}{2} + \sum_{n=1}^{\infty} K_n(\sqrt{B_o}) \left[\tilde{A}_n \cos(n\theta) + \tilde{B}_n \sin(n\theta) \right]
= -D_r(\theta) \left\{ \frac{\partial K_0(\sqrt{B_o}R)}{\partial R} \bigg|_{R=1} \frac{A_0}{2} + \sum_{n=1}^{\infty} \frac{\partial K_n(\sqrt{B_o}R)}{\partial R} \bigg|_{R=1} \left[A_n \cos(n\theta) + B_n \sin(n\theta) \right] \right\}, \tag{A6}$$

where A_n and B_n are given in (2.9).

In order to get explicit expressions for \tilde{A}_n and \tilde{B}_n , we use the following property of the Bessel functions K_n (Olver *et al.* 2010):

$$\frac{\partial K_n(\sqrt{B_o}R)}{\partial R} = -\frac{\sqrt{B_o}}{2} \left(K_{n-1}(\sqrt{B_o}R) + K_{n+1}(\sqrt{B_o}R) \right). \tag{A7}$$

Next, expanding the right-hand side of the equation in (A6) into Fourier series in the interval $\theta \in (0, 2\pi)$, we get exactly the expressions which were given in (2.12)–(2.13).

In order to check Fourier series convergence relative to the number of modes in the approximate solution, containing both the leading- and the first-order terms, we calculated the error which we denote by Err and define as

$$\text{Err} = h_c ||H(r, \theta; K = 50) - H(r, \theta; K)||_{\infty},$$
 (A8)

where $H(r, \theta)$ is as given in (2.6), (2.8) and (2.11), with the number of terms in the truncated series denoted by K and where $||\cdot||_{\infty}$ denotes the $L^{\infty}-$ norm in the two-dimensional domain $(r, \theta) \in (r_0, 3.5r_0) \times [0, 2\pi)$. In figure 9, we show the error graphs for the results shown in figure 6, corresponding to the hexagon, pentagon, square and triangle versus K. According to figure 9, it can be seen that in all cases the Fourier series converges exponentially relative to the number of modes in the series.

Appendix B. The solution in dimensional form

To obtain the dimensional solution, we first recall that the boundary conditions in dimensional notation are given by

$$h|_{r=r_0+d_r(\theta)} = \frac{w_0}{2} + \sum_{n=1}^{\infty} (q_n \sin{(n\theta)} + w_n \cos{(n\theta)}).$$
 (B1)

Now, we substitute the variables transformation given in (2.3) back into the dimensionless solution given in (2.8)–(2.9) and (2.11)–(2.13) and use the definition of B_o . Thus, we get that $h(r, \theta) = h_0(r, \theta) + \tilde{h}_1(r, \theta)$, where we denote for brevity

$$\tilde{h}_1(r,\theta) = \frac{\max_{\theta \in (0,2\pi)} |d_r(\theta)|}{r_0} h_1(r,\theta).$$
 (B2)

As to the leading-order solution, we get for $r > r_o$ that

$$h_0(r,\theta) = \frac{K_0\left(\sqrt{g\rho/\gamma}r\right)a_0}{2} + \sum_{n=1}^{\infty} K_n\left(\sqrt{g\rho/\gamma}r\right)\left[a_n\cos\left(n\theta\right) + b_n\sin\left(n\theta\right)\right], \quad (B3)$$

where a_n and b_n , the dimensional versions of A_n and B_n , are given by

$$a_n = \frac{w_n}{K_n(\sqrt{g\rho/\gamma}r_o)}$$
 and $b_n = \frac{q_n}{K_n(\sqrt{g\rho/\gamma}r_o)}$. (B4)

As to the first-order solution, we get for $r > r_o$ that

$$\tilde{h}_1(r,\theta) = \frac{K_0(\sqrt{g\rho/\gamma}r)\tilde{a}_0}{2} + \sum_{n=1}^{\infty} K_n(\sqrt{g\rho/\gamma}r) [\tilde{a}_n \cos(n\theta) + \tilde{b}_n \sin(n\theta)], \quad (B5)$$

where \tilde{a}_n and \tilde{b}_n , the dimensional versions of \tilde{A}_n and \tilde{B}_n , are given by

$$\tilde{a}_{n} = \frac{\sqrt{g\rho/\gamma}}{2\pi K_{n} (\sqrt{g\rho/\gamma} r_{o})} \int_{0}^{2\pi} g(\theta) \cos(n\theta) d\theta, \quad n = 0, 1, 2, \dots,$$

$$\tilde{b}_{n} = \frac{\sqrt{g\rho/\gamma}}{2\pi K_{n} (\sqrt{g\rho/\gamma} r_{o})} \int_{0}^{2\pi} g(\theta) \sin(n\theta) d\theta, \quad n = 1, 2, \dots,$$
(B6)

and where $g(\theta)$, the dimensional version of $G(\theta)$, is given by

$$g(\theta) = d_r(\theta) \left\{ \frac{\left(K_{-1}\left(\sqrt{g\rho/\gamma}r_o\right) + K_1\left(\sqrt{g\rho/\gamma}r_o\right)\right) a_0}{2} + \sum_{m=1}^{\infty} \left(K_{m-1}\left(\sqrt{g\rho/\gamma}r_o\right) + K_{m+1}\left(\sqrt{g\rho/\gamma}r_o\right)\right) \left[a_m \cos\left(m\theta\right) + b_m \sin\left(m\theta\right)\right] \right\}.$$
(B7)

Appendix C. The expressions for $\varepsilon D_r(\theta)$ for different shapes

In this section we shall give the expressions for $\varepsilon D_r(\theta)$ in four cases: equilateral hexagon, pentagon, square and triangle, which are shown in the insets of figure 5. In all cases the dimensionless radius of the inscribed circle is assumed to satisfy R = 1.

Let us start our discussion from equilateral hexagon, which is shown in the inset of figure 5(a). It is easy to verify that the sides of the hexagon, which we denote by L_i , i = 1, 2, ..., 6 (as indicated in the inset of figure 5a), are given by

$$L_{1}: y_{1} = \sqrt{3}x - 2,$$

$$L_{2}: y_{2} = -\sqrt{3}x - 2,$$

$$L_{3}: y_{3} = -\sqrt{3}x + 2,$$

$$L_{4}: y_{4} = \sqrt{3}x + 2,$$

$$L_{5}: y_{5} = 1, \qquad x = \frac{y_{5}}{\tan(\theta)} = \cot(\theta),$$

$$L_{6}: y_{6} = -1, \qquad x = \frac{y_{6}}{\tan(\theta)} = -\cot(\theta).$$
(C1)

Now, if we wish to express the sides L_i , i = 1, 2, 3, 4, in polar coordinates, namely in the form $(r_i \cos(\theta), r_i \sin(\theta))$, where θ is within the corresponding ranges, which are denoted by I_i , i = 1, 2, 3, 4, respectively, and are given in (C7), we need only to find r_i . However, according to (C1), it follows that

$$r_{i}(\theta) = \begin{cases} \frac{2}{\sqrt{3}\cos(\theta) - \sin(\theta)}, & i = 1, \\ -\frac{2}{\sqrt{3}\cos(\theta) + \sin(\theta)}, & i = 2, \\ \frac{2}{\sqrt{3}\cos(\theta) + \sin(\theta)}, & i = 3, \\ -\frac{2}{\sqrt{3}\cos(\theta) - \sin(\theta)}, & i = 4. \end{cases}$$
(C2)

Then, using the definition of $\varepsilon D_r(\theta)$, for sides of the form, $(r_i \cos(\theta), r_i \sin(\theta))$

$$\varepsilon D_r(\theta) = \sqrt{(1 - r_i(\theta))^2 \cos^2(\theta) + (1 - r_i(\theta))^2 \sin^2(\theta)} = -(1 - r_i(\theta)), \tag{C3}$$

with (C2), we readily find $\varepsilon D_r(\theta)$ for i = 1, 2, 3, 4. The correct sign of the square root in (C3) is minus, because if one refers to $D_r(\theta)$ as to a vector, it points from the circle towards the sides of the hexagon.

Next, expressing $\varepsilon D_r(\theta)$ for L_5 and L_6 (given in (C1)), where the corresponding ranges of θ are I_5 and I_6 , respectively, we get that

$$\varepsilon D_r(\theta) = \sqrt{(\cos(\theta) - \cot(\theta))^2 + (\sin(\theta) - 1)^2},$$
 (C4)

and

$$\varepsilon D_r(\theta) = \sqrt{\left(\cos\left(\theta\right) + \cot\left(\theta\right)\right)^2 + \left(\sin\left(\theta\right) + 1\right)^2}.$$
 (C5)

To summarise our results in (C2), (C4) and (C5) we may conclude that $\varepsilon D_r(\theta)$ in this case is given by

$$\varepsilon D_{r}(\theta) = \begin{cases} -1 + \frac{2}{\sqrt{3}\cos(\theta) - \sin(\theta)}, & \theta \in I_{1}, \\ -1 - \frac{2}{\sqrt{3}\cos(\theta) + \sin(\theta)}, & \theta \in I_{2}, \\ -1 + \frac{2}{\sqrt{3}\cos(\theta) + \sin(\theta)}, & \theta \in I_{3}, \\ -1 - \frac{2}{\sqrt{3}\cos(\theta) - \sin(\theta)}, & \theta \in I_{4}, \\ \sqrt{(\cos(\theta) - \cot(\theta))^{2} + (\sin(\theta) - 1)^{2}}, & \theta \in I_{5}, \\ \sqrt{(\cos(\theta) + \cot(\theta))^{2} + (\sin(\theta) + 1)^{2}}, & \theta \in I_{6}, \end{cases}$$
(C6)

where the various intervals are given by

$$I_{1} = \left[\frac{5\pi}{3}, 2\pi\right),$$

$$I_{2} = \left[\pi, \frac{4\pi}{3}\right),$$

$$I_{3} = \left[0, \frac{\pi}{3}\right),$$

$$I_{4} = \left[\frac{2\pi}{3}, \pi\right),$$

$$I_{5} = \left[\frac{\pi}{3}, \frac{2\pi}{3}\right),$$

$$I_{6} = \left[\frac{4\pi}{3}, \frac{5\pi}{3}\right).$$
(C7)

The function given in (C6) is shown in figure 5(a).

Next, we examine the expression for $\varepsilon D_r(\theta)$ in the case of the pentagon, which is shown in the inset of figure 5(b). Note that the length of the pentagon's side is

$$A = 2\tan\left(\pi/5\right). \tag{C8}$$

Hence, it is easy to verify that the sides of the pentagon, which we denote by \bar{L}_i , i = 1, 2, 3, 4, 5 (as indicated in the inset of figure 5b) are given by

$$\bar{L}_{i}: \quad y_{i} = a_{i}x - \left(1 + \frac{A}{2\tan(\pi/10)}\right), \quad i = 1, 2,$$

$$\bar{L}_{i}: \quad y_{i} = a_{i}x + \frac{1}{\sin(3\pi/10)}, \qquad i = 3, 4,$$

$$\bar{L}_{5}: \quad y_{5} = -1, \qquad x = \frac{y_{5}}{\tan(\theta)} = -\cot(\theta),$$
(C9)

where

$$a_1 = \tan\left(\frac{2\pi}{5}\right), \quad a_2 = -\tan\left(\frac{2\pi}{5}\right), \quad a_3 = \tan\left(\frac{4\pi}{5}\right), \quad a_4 = -\tan\left(\frac{4\pi}{5}\right). \quad (C10)$$

Now, if we wish to express the sides \bar{L}_i , i = 1, 2, 3, 4, in polar coordinates, namely in the form $(r_i \cos(\theta), r_i \sin(\theta))$, where θ is within the corresponding ranges, which are denoted

by I_i , i = 1, 2, 3, 4, respectively, and are given in (C16), we need only to find r_i . However, according to (C9), it follows that

$$a_i r_i \cos(\theta) - \left(1 + \frac{A}{2 \tan(\pi/10)}\right) = r_i \sin(\theta), \quad i = 1, 2,$$
 (C11)

and

$$a_i r_i \cos(\theta) + \frac{1}{\sin(3\pi/10)} = r_i \sin(\theta), \quad i = 3, 4.$$
 (C12)

Hence,

$$r_{i}(\theta) = \begin{cases} -\frac{1 + \frac{A}{2 \tan{(\pi/10)}}}{\sin{(\theta)} - \tan{(2\pi/5)}\cos{(\theta)}}, & i = 1, \\ \frac{1 + \frac{A}{2 \tan{(\pi/10)}}}{\sin{(\theta)} + \tan{(2\pi/5)}\cos{(\theta)}}, & i = 2, \\ \frac{1}{\sin{(3\pi/10)} \left[\sin{(\theta)} - \tan{(4\pi/5)}\cos{(\theta)}\right]}, & i = 3, \\ \frac{1}{\sin{(3\pi/10)} \left[\sin{(\theta)} + \tan{(4\pi/5)}\cos{(\theta)}\right]}, & i = 4. \end{cases}$$
(C13)

Then, using the formula in (C3) with (C13), we readily find $\varepsilon D_r(\theta)$ for i = 1, 2, 3, 4. Finally, expressing $\varepsilon D_r(\theta)$ for \bar{L}_5 (given in (C9)), we get that

$$\varepsilon D_r(\theta) = \sqrt{\left(\cos\left(\theta\right) + \cot\left(\theta\right)\right)^2 + \left(\sin\left(\theta\right) + 1\right)^2}.$$
 (C14)

To summarise our results in (C13) and (C14), we may conclude that $\varepsilon D_r(\theta)$ in this case is given by

$$\varepsilon D_{r}(\theta) = \begin{cases}
-1 - \frac{1 + \frac{A}{2\tan(\pi/10)}}{\sin(\theta) - \tan(2\pi/5)\cos(\theta)}, & \theta \in I_{1}, \\
-1 - \frac{1 + \frac{A}{2\tan(\pi/10)}}{\sin(\theta) + \tan(2\pi/5)\cos(\theta)}, & \theta \in I_{2}, \\
-1 + \frac{1}{\sin(3\pi/10)\left[\sin(\theta) - \tan(4\pi/5)\cos(\theta)\right]}, & \theta \in I_{3}, \\
-1 + \frac{1}{\sin(3\pi/10)\left[\sin(\theta) + \tan(4\pi/5)\cos(\theta)\right]}, & \theta \in I_{4}, \\
\sqrt{(\cos(\theta) + \cot(\theta))^{2} + (\sin(\theta) + 1)^{2}}, & \theta \in I_{5},
\end{cases} (C15)$$

where the various intervals are given by

$$I_{1} = \left[0, \frac{\pi}{10}\right] \cup \left[\frac{17\pi}{10}, 2\pi\right),$$

$$I_{2} = \left(\frac{9\pi}{10}, \frac{13\pi}{10}\right],$$

$$I_{3} = \left(\frac{\pi}{10}, \frac{\pi}{2}\right],$$

$$I_{4} = \left(\frac{\pi}{2}, \frac{9\pi}{10}\right],$$

$$I_{5} = \left(\frac{13\pi}{10}, \frac{17\pi}{10}\right).$$
(C16)

The function given in (C15) is shown in figure 5(b).

Now consider the expression for $\varepsilon D_r(\theta)$ in the case of the square, which is shown in the inset of figure 5(c). It is easy to verify that the sides of the square, which we denote by \tilde{L}_i , i=1,2,3,4 (as indicated in the inset of figure 5c), are given by

$$\tilde{L}_{1}: \quad x = 1, \qquad y = x \tan(\theta) = \tan(\theta),
\tilde{L}_{2}: \quad x = -1, \qquad y = x \tan(\theta) = -\tan(\theta),
\tilde{L}_{3}: \quad y = 1, \qquad x = \frac{y}{\tan(\theta)} = \cot(\theta),
\tilde{L}_{4}: \quad y = -1, \qquad x = \frac{y}{\tan(\theta)} = -\cot(\theta).$$
(C17)

Hence, the distance $\varepsilon D_r(\theta)$ between the circle and \tilde{L}_1 is given by

$$\varepsilon D_r(\theta) = \sqrt{(\cos(\theta) - 1)^2 + (\sin(\theta) - \tan(\theta))^2},$$
 (C18)

where the corresponding range of θ is given in I_1 , see (C20).

The rest of the sides of the square are treated similarly, thus overall resulting that for $\theta \in [0, 2\pi)$, $\varepsilon D_r(\theta)$ is given by

$$\varepsilon D_{r}(\theta) = \begin{cases} \sqrt{\left(\cos\left(\theta\right) - 1\right)^{2} + \left(\sin\left(\theta\right) - \tan\left(\theta\right)\right)^{2}}, & \theta \in I_{1}, \\ \sqrt{\left(\cos\left(\theta\right) + 1\right)^{2} + \left(\sin\left(\theta\right) + \tan\left(\theta\right)\right)^{2}}, & \theta \in I_{2}, \\ \sqrt{\left(\cos\left(\theta\right) - \cot\left(\theta\right)\right)^{2} + \left(\sin\left(\theta\right) - 1\right)^{2}}, & \theta \in I_{3}, \\ \sqrt{\left(\cos\left(\theta\right) + \cot\left(\theta\right)\right)^{2} + \left(\sin\left(\theta\right) + 1\right)^{2}}, & \theta \in I_{4}, \end{cases}$$
(C19)

where

$$I_{1} = [0, 0.25\pi) \cup (1.75\pi, 2\pi),$$

$$I_{2} = [0.75\pi, 1.25\pi),$$

$$I_{3} = [0.25\pi, 0.75\pi),$$

$$I_{4} = [1.25\pi, 1.75\pi].$$
(C20)

The function given in (C19) is shown in figure 5(c).

Finally, we derive the expression for $\varepsilon D_r(\theta)$ in the case of the triangle, which is shown in the inset of figure 5(d). It is easy to verify that the sides of the triangle, which we denote by \hat{L}_i , i = 1, 2, 3 (as indicated in the inset of figure 5d), are given by

$$\hat{L}_i: \quad y_i = a_i x + \frac{1}{\sin(\pi/6)}, \quad i = 1, 2,$$

$$\hat{L}_3: \quad y_3 = -1, \qquad \qquad x = \frac{y_3}{\tan(\theta)} = -\cot(\theta).$$
(C21)

where

$$a_1 = \tan(2\pi/3) = -\sqrt{3}$$
 and $a_2 = \tan(\pi/3) = \sqrt{3}$. (C22)

Now, if we wish to express the sides \hat{L}_i , i = 1, 2, in polar coordinates, namely in the form $(r_i \cos(\theta), r_i \sin(\theta))$, where θ is within the corresponding ranges, which are denoted by I_i , i = 1, 2, respectively, and are given in (C27), we need only to find r_i . However, according to (C21), it follows that

$$a_i r_i \cos(\theta) + \frac{1}{\sin(\pi/6)} = r_i \sin(\theta), \quad i = 1, 2.$$
 (C23)

Hence, we may conclude that

$$r_{i}(\theta) = \frac{1}{\sin(\pi/6)(\sin(\theta) - a_{i}\cos(\theta))}$$

$$= \frac{1}{2(\sin(\theta) \pm \sqrt{3}\cos(\theta))}, \qquad i = 1, 2,$$
(C24)

where $\sqrt{3}$ corresponds to i=1 and $-\sqrt{3}$ corresponds to i=2. Then, using the formula in (C3) with (C24), we readily find $\varepsilon D_r(\theta)$ for i=1,2.

Finally, expressing $\varepsilon D_r(\theta)$ for \hat{L}_3 (given in (C21)), where the corresponding range of θ is I_3 (given in (C27)), we get that

$$\varepsilon D_r(\theta) = \sqrt{(\cos(\theta) + \cot(\theta))^2 + (\sin(\theta) + 1)^2}.$$
 (C25)

To summarise our results in (C24) and (C25), we may conclude that $\varepsilon D_r(\theta)$ in this case is given by

$$\varepsilon D_r(\theta) = \begin{cases} -1 + \frac{1}{2(\sqrt{3}\cos(\theta) + \sin(\theta))}, & \theta \in I_1, \\ -1 - \frac{1}{2(\sqrt{3}\cos(\theta) - \sin(\theta))}, & \theta \in I_2, \\ \sqrt{(\cos(\theta) + \cot(\theta))^2 + (\sin(\theta) + 1)^2}, & \theta \in I_3, \end{cases}$$
(C26)

where the various intervals are given by

$$I_{1} = \left[0, \frac{\pi}{2}\right] \cup \left[\frac{11\pi}{6}, 2\pi\right),$$

$$I_{2} = \left(\frac{\pi}{2}, \frac{7\pi}{6}\right],$$

$$I_{3} = \left(\frac{7\pi}{6}, \frac{11\pi}{6}\right).$$
(C27)

The function given in (C26) is shown in figure 5(d).

Appendix D. Estimation of the error in contact inclination angle at the particle boundary due to the liquid height uncertainty

The inclination angle of the meniscus near the particle boundary is denoted by α and may be found according to the formula

$$\alpha = \operatorname{arccot}\left(\frac{\partial h}{\partial r}\Big|_{r=r_o+d_r(\theta)}\right) = \operatorname{arccot}\left(\frac{h_c}{r_0} \left.\frac{\partial H}{\partial R}\Big|_{R=1+\varepsilon D_r(\theta)}\right),\tag{D1}$$

where we used the scaling parameters which were defined in (2.3). Now, from the expansion in (2.6), it easily follows that

$$\frac{\partial H}{\partial R} = \frac{\partial H_0}{\partial R} + \varepsilon \frac{\partial H_1}{\partial R} + O(\varepsilon^2). \tag{D2}$$

According to the solution for the leading-order problem, which was given in (2.8)–(2.9), and the formula for the derivative of the Bessel functions given in (A7), it follows that

$$\frac{\partial H_0}{\partial R} = -\frac{A_0 \sqrt{B_o}}{4} \left(K_{-1} \left(\sqrt{B_o} R \right) + K_1 \left(\sqrt{B_o} R \right) \right) - \frac{\sqrt{B_o}}{2} \sum_{n=1}^{\infty} \left[A_n \cos(n\theta) + B_n \sin(n\theta) \right] \left(K_{n+1} \left(\sqrt{B_o} R \right) + K_{n-1} \left(\sqrt{B_o} R \right) \right).$$
(D3)

Note that, since, according to (2.11), the expression for $H_1(R, \theta)$ is the same as for $H_0(R, \theta)$, except that A_0 , A_n and B_n , $n = 1, 2, 3, \ldots$, are replaced with \tilde{A}_0 , \tilde{A}_n and \tilde{B}_n , respectively, also the expression for $\partial H_1/\partial R$ is the same as for $\partial H_0/\partial R$, except that A_0 , A_n and B_n , $n = 1, 2, 3, \ldots$, are replaced with \tilde{A}_0 , \tilde{A}_n and \tilde{B}_n , respectively.

In order to assess the effect of uncertainty of the water level in the experiments, which is ± 0.05 mm, on the inclination angle α , we calculated α by using the equations in (D1)–(D3) and the derivative $\partial H_1/\partial R$ for 3 representative points, which we denote by P_1 , P_2 and P_3 (see figure 10) located on the boundaries of the square and hexagonal-shaped particles. One point was chosen close to the centre of the particles' edge, one is chosen closer to the corner and one was randomly chosen in between them. This calculation was repeated for three cases: (i) the centreline of the particle is the same as the liquid–gas interface height at $r \to \infty$, (ii) the centreline of the particle is above the liquid–gas interface height at $r \to \infty$ by 0.05 mm, and (iii) the centreline of the particle is below the liquid–gas interface height at $r \to \infty$ by 0.05 mm. Our results are summarised in table 1.

According to the representative results shown in table 1, it can be seen that the uncertainty of ± 0.05 mm in the measurement of the liquid–gas interface at far field results in the error of the order of ± 1 % in the inclination angle of the meniscus.

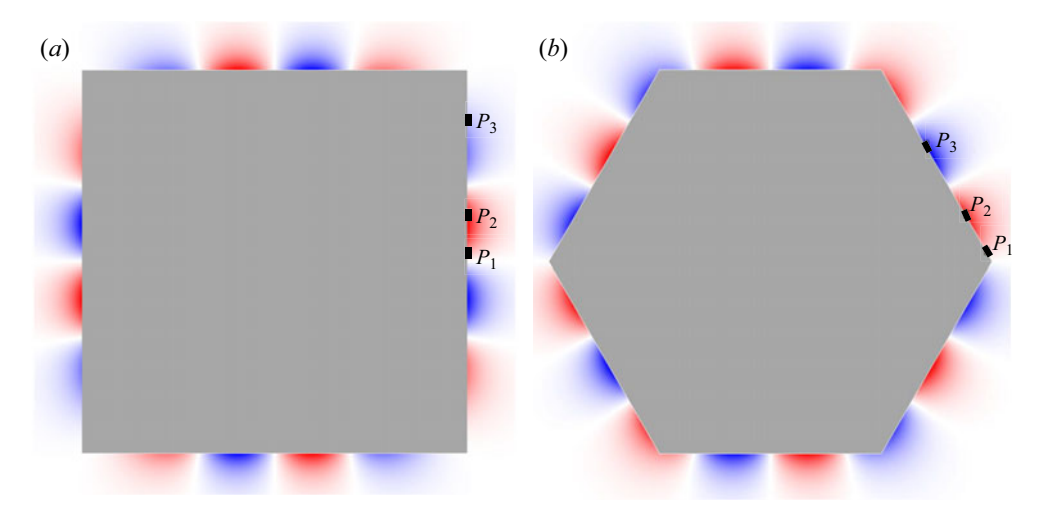


Figure 10. The liquid–gas interface shape for a square and a hexagonal-shaped particles, for which we calculated the inclination angles in table 1, where the points P_1 , P_2 and P_3 are indicated.

Particle shape/point	Angle α in case (i)	Angle α in case (ii)	Angle α in case (iii)
Square/P ₁	-86.0794°	-85.08°	-87.0812°
Square/ P_2	-74.9464°	-73.9914°	-75.9101°
Square/P ₃	86.607°	87.0784°	86.1361°
Hexagon/ P_1	-87.2804°	-86.4783°	-88.0835°
Hexagon/ P_2	-77.0952°	−76.1403°	-78.0574°
Hexagon/P ₃	76.4048°	77.4613°	-75.3577°

Table 1. The inclination angle α , calculated according to (D1), on 3 points P_1 , P_2 and P_3 in three cases: case (i), case (ii), and case (iii) where in case (i) the centerline of the particle is the same as of the liquid-gas interface at infinity, in case (ii) the centerline is 0.05 mm above the liquid-gas interface at infinity, and in case (iii) the centerline is 0.05 mm below the liquid-gas interface at infinity.

Appendix E. The second-order expansion

Here, we derive an expression for the second-order term in the expansion of $H(R, \theta)$ in asymptotic series. Similarly to (2.5), we expand $(H_0 + \varepsilon H_1 + \varepsilon^2 H_2)|_{R=1+\varepsilon D_r(\theta)}$ into a Taylor series in ε around $\varepsilon = 0$, as follows:

$$\left(H_{0} + \varepsilon H_{1} + \varepsilon^{2} H_{2}\right)\big|_{R=1+\varepsilon D_{r}(\theta)} = H_{0}\big|_{R=1} + \varepsilon \left(H_{1} + D_{r}(\theta) \frac{\partial H_{0}}{\partial R}\right)\Big|_{R=1} + \varepsilon^{2} \left(H_{2} + D_{r}(\theta) \frac{\partial H_{1}}{\partial R} + 0.5 D_{r}^{2}(\theta) \frac{\partial^{2} H_{0}}{\partial R^{2}}\right)\Big|_{R=1} + O(\varepsilon^{3}).$$
(E1)

Next, similarly to the discussion for $H_1(R, \theta)$ (see (2.10)), we get at the second, $O(\varepsilon^2)$, order the following problem:

$$R^{2} \frac{\partial^{2} H_{2}}{\partial R^{2}} + R \frac{\partial H_{2}}{\partial R} + \frac{\partial^{2} H_{2}}{\partial \theta^{2}} - B_{o} R^{2} H_{2} = 0,$$

$$H_{2}|_{R=1} = -\left(D_{r}(\theta) \frac{\partial H_{1}}{\partial R} + 0.5 D_{r}^{2}(\theta) \frac{\partial^{2} H_{0}}{\partial R^{2}}\right)\Big|_{R=1},$$

$$H_{2}|_{R \to \infty} = 0.$$
(E2)

Note that, since the equation for H_2 as given in (E2) is exactly of the same form as the equation for H_0 and H_1 , by using the same procedure as described above, we get the same general solution for H_2 as for H_0 and H_1 , see (2.8) and (2.11), namely

$$H_2(R,\theta) = \frac{K_0(\sqrt{B_o}R)\hat{A}_0}{2} + \sum_{n=1}^{\infty} K_n(\sqrt{B_o}R) \left[\hat{A}_n\cos\left(n\theta\right) + \hat{B}_n\sin\left(n\theta\right)\right], \quad (E3)$$

where the constants \hat{A}_n and \hat{B}_n are determined by using the boundary conditions in (E2). In order to determine the constants \hat{A}_n and \hat{B}_n explicitly, analogously to the coefficients \tilde{A}_n and \tilde{B}_n appearing in the Fourier series of $H_1(R, \theta)$, see (2.12), we get now that

$$\hat{A}_{n} = \frac{\sqrt{B_{o}}}{2\pi K_{n}(\sqrt{B_{o}})} \int_{0}^{2\pi} \left[\tilde{G}(\theta) - \hat{G}(\theta)\right] \cos(n\theta) d\theta, \quad n = 0, 1, 2, \dots,$$

$$\hat{B}_{n} = \frac{\sqrt{B_{o}}}{2\pi K_{n}(\sqrt{B_{o}})} \int_{0}^{2\pi} \left[\tilde{G}(\theta) - \hat{G}(\theta)\right] \sin(n\theta) d\theta, \quad n = 1, 2, \dots,$$
(E4)

where for brevity we use the following notation:

$$\tilde{G}(\theta) = D_{r}(\theta) \left\{ \frac{\left(K_{-1}(\sqrt{B_{o}}) + K_{1}(\sqrt{B_{o}})\right) \tilde{A}_{0}}{2} + \sum_{m=1}^{\infty} \left(K_{m-1}(\sqrt{B_{o}}) + K_{m+1}(\sqrt{B_{o}})\right) \left[\tilde{A}_{m} \cos(m\theta) + \tilde{B}_{m} \sin(m\theta)\right] \right\},$$
(E5)

and

$$\hat{G}(\theta) = \frac{D_r^2(\theta)\sqrt{B_o}}{4} \left\{ \frac{\left(K_{-2}(\sqrt{B_o}) + 2K_0(\sqrt{B_o}) + K_2(\sqrt{B_o})\right)A_0}{2} + \sum_{m=1}^{\infty} \left(K_{m-2}(\sqrt{B_o}) + 2K_m(\sqrt{B_o}) + K_{m+2}(\sqrt{B_o})\right) \right.$$

$$\times \left[A_m \cos(m\theta) + B_m \sin(m\theta)\right] \right\}.$$
(E6)

Note that, in the derivation of the expression in (E6), we used (A7), according to which it easily follows that

$$\frac{\partial^2 K_n(\sqrt{B_o}R)}{\partial R^2} = \frac{B_o}{4} \left(K_{n-2}(\sqrt{B_o}R) + 2K_n(\sqrt{B_o}R) + K_{n+2}(\sqrt{B_o}R) \right). \tag{E7}$$

REFERENCES

- BEATUS, T., BAR-ZIV, R.H. & TLUSTY, T. 2012 The physics of 2D microfluidic droplet ensembles. *Phys. Rep* **516** (3), 103–145.
- BINKS, B.P. & HOROZOV, T.S. 2006 Colloidal Particles at Liquid Interfaces. Cambridge University Press.
- BOTTO, L., LEWANDOWSKI, E.P., CAVALLARO, M. & STEBE, K.J. 2012 Capillary interactions between anisotropic particles. *Soft Matter* **8** (39), 9957–9971.
- BOWDEN, N., TERFORT, A., CARBECK, J. & WHITESIDES, G.M. 1997 Self-assembly of mesoscale objects into ordered two-dimensional arrays. *Science* **276** (5310), 233–235.
- BOWDEN, N.B., CHOI, I.S., GRZYBOWSKI, B.A. & WHITESIDES, G.M. 1999 Mesoscale self-assembly of hexagonal plates using lateral capillary forces: synthesis using the capillary bond. *J. Am. Chem. Soc.* 121, 5373–5391,653.
- BUCARO, M.A., KOLODNER, P.R., TAYLOR, J.A., SIDORENKO, A., AIZENBERG, J. & KRUPENKIN, T.N. 2009 Tunable liquid optics: electrowetting-controlled liquid mirrors based on self-assembled janus tiles. *Langmuir* 25, 3876–3879.
- Bush, J.W.M. & Hu, D.L. 2006 Walking on water: biolocomotion at the interface. *Annu. Rev. Fluid Mech.* **38** (1), 339–369.
- CHAN, D.Y.C., HENRY, J.D. & WHITE, L.R. 1981 The interaction of colloidal particles collected at fluid interfaces. J. Colloid Interface Sci. 79 (2), 410–418.
- DANOV, K.D. & KRALCHEVSKY, P.A. 2010 Capillary forces between particles at a liquid interface: general theoretical approach and interactions between capillary multipoles. *Adv. Colloid Interface Sci.* **154** (1), 91–103.
- DANOV, K.D., KRALCHEVSKY, P.A., NAYDENOV, B.N. & BRENN, G. 2005 Interactions between particles with an undulated contact line at a fluid interface: capillary multipoles of arbitrary order. *J. Colloid Interface Sci.* 287 (1), 121–134.
- DELENS, M., COLLARD, Y. & VANDEWALLE, N. 2023 Induced capillary dipoles in floating particle assemblies. *Phys. Rev. Fluids* **8**, 074001.
- EATSON, J.L., MORGAN, S.O., HOROZOV, T.S. & BUZZA, D.M.A. 2024 Programmable 2D materials through shape-controlled capillary forces. *Proc. Natl Acad. Sci. USA* 121 (35), e2401134121.
- FORTH, J., KIM, P.Y., XIE, G., LIU, X., HELMS, B.A. & RUSSELL, T.P. 2019 Building reconfigurable devices using complex liquid–fluid interfaces. *Adv. Mater.* 31 (18), 1806370.
- GAO, X. & JIANG, L. 2004 Water-repellent legs of water striders. Nature 432, 36.
- GAT, A.D. & GHARIB, M. 2013 Elasto-capillary coalescence of multiple parallel sheets. *J. Fluid Mech.* **723**, 692–705.
- DE GENNES, P.G., BROCHARD-WYART, F. & QUERE, D. 2003 Capillarity and Wetting Phenomena: Drops, Bubbles, Pearls, Waves. Springer New York.
- HINSCH, K.D. 1978 Holographic interferometry of surface deformations of transparent fluids. Appl. Opt. 17 (19), 3101–3107.
- JANSSENS, S.D., CHAURASIA, V. & FRIED, E. 2017 Effect of a surface tension imbalance on a partly submerged cylinder. *J. Fluid Mech.* **830**, 369–386.
- KOENS, L., WANG, W., SITTI, M. & LAUGA, E. 2019 The near and far of a pair of magnetic capillary disks. Soft Matter 15, 1497–1507.
- Kralchevsky, P.A. & Denkov, N.D. 2001 Capillary forces and structuring in layers of colloid particles. *Curr. Opin. Colloid Interface Sci.* 6 (4), 383–401.
- Kralchevsky, P.A. & Nagayama, K. 1994 Capillary forces between colloidal particles. *Langmuir* 10 (1), 23–36.
- Kralchevsky, P.A. & Nagayama, K. 2000 Capillary interactions between particles bound to interfaces, liquid films and biomembranes. *Adv. Colloid Interface Sci.* **85** (2), 145–192.
- LANDAU, L. & LIFSHITZ, E. 1987 In Fluid Mechanics, vol. 6. Elsevier.
- LEAL, L.G. 2007 Advanced Transport Phenomena: Fluid Mechanics and Convective Transport Processes. vol. 7. Cambridge University Press.
- LEWANDOWSKI, E.P., BERNATE, J.A., SEARSON, P.C. & STEBE, K.J. 2008 Rotation and alignment of anisotropic particles on nonplanar interfaces. *Langmuir* 24, 9302–9307.
- LOUDET, J.C., ALSAYED, A.M., ZHANG, J. & YODH, A.G. 2005 Capillary interactions between anisotropic colloidal particles. *Phys. Rev. Lett.* **94**, 018301.
- LOUDET, J.C., YODH, A.G. & POULIGNY, B. 2006 Wetting and contact lines of micrometer-sized ellipsoids. *Phys. Rev. Lett.* **97**, 018304.
- LUCASSEN, J. 1992 Capillary forces between solid particles in fluid interfaces. *Colloid. Surface.* **65** (2), 131–137.

- MANSFIELD, E.H., SEPANGI, H.R. & EASTWOOD, E.A. 1997 Equilibrium and mutual attraction or repulsion of objects supported by surface tension. *Phil. Trans. A Math. Phys. Engng Sci.* **355** (1726), 869–919.
- NICOLSON, M.M. 1949 The interaction between floating particles. *Math. Proc. Camb. Phil. Soc.* **45** (2), 288–295.
- VAN NIEROP, E.A., STIJNMAN, M.A. & HILGENFELDT, S. 2005 Shape-induced capillary interactions of colloidal particles. *Europhys. Lett.* **72** (4), 671.
- OLVER, F.W.J., LOZIER, D.W., BOISVERT, R.F. & CLARK, C.W. 2010 NIST Handbook of Mathematical Functions. Cambridge University Press.
- POTY, M., LUMAY, G. & VANDEWALLE, N. 2014 Customizing mesoscale self-assembly with three-dimensional printing. *New J. Phys.* **16** (2), 023013.
- PRAKASH, S., PERRIN, H. & BOTTO, L. 2024 Buckling of a monolayer of platelike particles trapped at a fluid-fluid interface. *Phys. Rev. E* **109**, 014801.
- ROTMAN, A. 2009 Verification of the influence of surface energies on the effective mobility, Master's thesis. Mathematics Department, Technion.
- SINGER, A. 2004 Maximum entropy formulation of the Kirkwood superposition approximation. *J. Chem. Phys.* **121** (8), 3657–3666.
- SINGH, P. & JOSEPH, D.D. 2005 Fluid dynamics of floating particles. J. Fluid Mech. 530, 31-80.
- SOLIGNO, G., DIJKSTRA, M. & VAN ROIJ, R. 2016 Self-assembly of cubes into 2D hexagonal and honeycomb lattices by hexapolar capillary interactions. *Phys. Rev. Lett.* **116**, 258001.
- TAN, D., ZHANG, F. & ZHOU, X. 2022 Surface tension force on a partially submerged horizontal concave cylinder. *J. Fluid Mech.* **950**, A15.
- TAVACOLI, J.W., KATGERT, G., KIM, E.G., CATES, M.E. & CLEGG, P.S. 2012 Size limit for particle-stabilized emulsion droplets under gravity. *Phys. Rev. Lett.* **108**, 268306.
- VELLA, D. & MAHADEVAN, L. 2005 The 'Cheerios effect'. Am. J. Phys. 73 (9), 817-825.
- WHITESIDES, G.M. & BONCHEVA, M. 2002 Beyond molecules: self-assembly of mesoscopic and macroscopic components. Proc. Natl Acad. Sci. USA 99 (8), 4769–4774.
- WHITESIDES, G.M. & GRZYBOWSKI, B. 2002 Self-assembly at all scales. Science 295 (5564), 2418–2421.
- WOLFE, D.B., SNEAD, A., MAO, C., BOWDEN, N.B. & WHITESIDES, G.M. 2003 Mesoscale self-assembly: capillary interactions when positive and negitive menisci have similar amplitudes. *Langmuir* 19, 2206–2214,831.
- YAO, L., BOTTO, L., CAVALLARO, M., Jr, BLEIER, B.J., GARBIN, V. & STEBE, K.J. 2013 Near field capillary repulsion. *Soft Matter* **9**, 779–786.
- YAO, L., SHARIFI-MOOD, N., LIU, I.B. & STEBE, K.J. 2015 Capillary migration of microdisks on curved interfaces. J. Colloid Interface Sci. 449, 436–442.
- ZHANG, F., ZHOU, X. & ZHU, C. 2018 Effects of surface tension on a floating body in two dimensions. J. Fluid Mech. 847, 489–519.
- ZHANG, SONG 2018 High-speed 3D shape measurement with structured light methods: a review. *Opt. Lasers Eng.* **106**, 119–131.
- ZHANG, W., ZHANG, F., TAN, D. & ZHOU, X. 2023 Exotic flotation theory with new method for floating stability analysis. J. Fluid Mech. 973, A25.
- ZHANG, W. & ZHOU, X. 2023 Equilibria and stabilities of a confined floating cylinder. J. Fluid Mech. 954, A22.